Broadband Metamaterial Absorbers for Organic Solar Cells: A Review

Diyaree O. Kakil¹, Fahmi F. Muhammadsharif^{1†} and Yadgar I. Abdulkarim²

¹Department of Physics, Faculty of Science and Health, Koya University, Danielle Mitterrand Boulevard, Koya KOY45, Kurdistan Region – F.R. Iraq

²Physics Department, College of Science, Charmo University, 46023 Chamchamal, Sulaimania, Kurdistan Region – F.R. Iraq

Abstract—Organic solar cells (OSCs) often suffer from weak absorption in the visible and infrared spectrum, which directly restricts their efficiency. Since light harvesting is central to solar conversion, improving absorption across a broad range is critical. Broadband metamaterial absorbers (BMMAs) present a promising solution by enhancing light-matter interaction and extending absorption over a broader spectrum. This improvement directly makes the process of converting energy more efficient. This review aims to systematically examine the recent progress of metamaterial absorbers (MMAs), highlighting broadband, polarizationindependent, and wide-angle designs areas that remain unexplored in recent reviews. Different categories of strategies, such as planar, vertical, lumped-element, and nanostructured plasmonic designs, are discussed to highlight how material choice and design geometry affect absorption. In addition, it describes the physical concepts of perfect absorption and assesses how applicable they are to OSC integration. Our analysis shows that the most of the progress has been theoretical approaches with a limited experiment. These studies demonstrate that BMMAs have an excellent opportunity to significantly improve energy conversion efficiency. At the same time, most challenges remain, like scalability, material losses, and easy integration into OGCs. This research also points out that there are future investigations into affordable, low-loss materials that can be easily integrated. Overall, this study emphasizes how important MMBAs are to advancing the efficiency and sustainability of nextgeneration OSCs.

Index Terms—Broadband absorbers, Metamaterials, Organic solar cells, Photovoltaic efficiency, Plasmonic.

I. Introduction

Solar energy is an eco-friendly source of energy, offering an excellent renewable power supply and green energy source. It significantly contributes to sustainable development

ARO-The Scientific Journal of Koya University Vol. XIII, No.2(2025), Article ID: ARO.12025. 255 pages DOI: 10.14500/aro.12025

Received: 04 July 2025; Accepted: 21 August 2025
Regular Review Paper; Published: 06 November 2025

†Corresponding author's e-mail: fahmi.fariq@koyauniversity.org
Copyright © 2025 Diyaree O. Kakill, Fahmi F. Muhammadsharif
and Yadgar I. Abdulkarim. This is an open-access article distributed
under the Creative Commons Attribution License
(CC BY-NC-SA 4.0).



and energy solutions (Kishore, Kumar and Ippili, 2025). In recent years, there has been a significant focus on the development and advancement of inorganic solar cells, leading to their widespread production around the world (Lazaroiu, et al., 2023). However, the high cost associated with these technologies has motivated researchers toward more economical alternatives of organic-based solar cells (Solak and Irmak, 2023) Organic solar cells (OSCs) are known for their versatility, low manufacturing costs, and lightweight nature. They have become a desirable choice for a variety of applications. However, despite these many advantages, the performance of OSCs remains one of the critical challenges in terms of power conversion efficiency (PCE) and environmental stability while operation (Tegegne, Nchinda and Krüger, 2025). Poor light absorption and charge transport delays have caused OSCs to lag behind their inorganic counterparts (Jain, et al., 2024, Carrillo-Sendejas and Maldonado, 2025). Metamaterials (MMs) are new manmade materials with unique electromagnetic properties, known for their ability to manipulate the interaction of electromagnetic waves (Landy, et al., 2008). MMs present a promising solution for improving the efficiency performance of OSC. Adding the MM structure to the cell's active layer improves how light interacts with the organic active layers. It has the potential to broaden the absorbance spectrum rate and improve quantum efficiency. In recent years, MMs have received significant attention for their potential role in enhancing solar cell efficiency by manipulating light in unconventional ways (Ali, Mitra and Aïssa, 2022).

In a research review (Ahmad, et al., 2024), authors explored MM applications in various renewable energy sectors, including solar cells. The review paper discusses specific challenges in traditional solar cells, including insufficient photon absorption due to silicon limitations, and presents potential solutions, including multilayer waveguides or multiresonators structures to enhance light trapping and absorption. Numerical simulation indicates that specific designs can improve the efficiency of solar cell from 7.4% to 12% for certain structure. Furthermore, another review (Prasada, et al., 2021) highlighted that the wide-angle absorption and broadband of such engineered material can be matched with solar spectrum, resulting in increased

ARO p-ISSN: 2410-9355, e-ISSN: 2307-549X

absorption at a variety of incoming angles, which is highly crucial for solar cells.

However, there are yet challenges with achieving a broadband MM with prefect absorption and hence solar absorption in a narrow range of wavelength reduces the device effectiveness. For example, semicircular structure that consists of nickel (Ni) and silicon nitride (SiN) showed about 77% of absorption in solar spectrum, while about 84% was in the visible region (Liu, et al., 2012a). In another study, the role of MM in energy harvesting devices was discussed (Góra and Łopato, 2023). It has been claimed that a structure of metal-dielectric-metal shows a broadband absorption in the visible region, independent of polarization and incoming angles. Moreover, the structure showed an absorption efficiency of about 99% across the spectrum, specifically within the range of 456.62-677.73 nm (Kumar, Singh and Pandey, 2022). A recent design was also demonstrated with an ultra-broadband characteristics, showing a bandwidth of 1.78 µm and 90% of absorption efficiency (Cen, et al., 2025).

It was evident that previous review papers have often discussed MM absorbers (MMAs) in the broader context of their applications in the renewable energy sector or ecofriendly technologies, including inorganic solar cells. To the best of our knowledge, there is no specific review dedicated to explore the utilization of perfect MMAs for OSCs and their implication in the new emerging OSC technology. Therefore, the present work focuses on broadband absorbers that are independent of polarization and incident angle, with a particular attention to their applicability to OSCs. This focused review aims to reveal the unexplored areas of the MMs and to emphasize the necessity for more investigations in the field of OSC. As such, we will delve into the fundamental properties of MMs and examine their absorption behavior in metal-insulator-metal (MIM) configurations. To explain the absorption process, we present the physical mechanisms of broadband MM, which is important for the application of OSCs. Consequently, the integration of broadband MMs into OSCs with different designs is elaborated.

II. THE NOTION OF MMS

In macroscopic optics, the refractive index (n) of a material is typically defined as n = c/v, where c represents the speed of light in vacuum, and v refers to the speed of an electromagnetic wave within the medium. For a linear, isotropic, homogeneous, and charge-free lossy dielectric material, the macroscopic Maxwell's equations are expressed as (Jackson, 1999, Cheng, 1989).

$$n^2 = \mu_r \, \varepsilon_r \tag{1}$$

Where ε_r represents the relative dielectric permittivity, and μ_r refers to the relative magnetic permeability of the medium. Typically, in natural optical materials, both are positive, exhibiting positive refractive indices (n). However, Victor Veselago (Veselago, 1967) in 1968 introduced the concept of a medium with simultaneous negative permittivity

and permeability. He predicted that such a medium should be regarded as possessing a negative refractive index. In addition, he predicted consequential effects such as reversed Snell's refraction and a reversed Doppler shift. Subsequent experimental studies, decades later, validated his theoretical prediction, confirming those effects. Following the Veselago framework, the classification of materials is based on the signs of ε_{μ} and μ_{μ} , providing a clear distinction between conventional dielectric, metals, and MM, as shown in Fig. 1. Fig. 1 presents the material classification based on permittivity and permeability (Wang and Karaaslan, 2023). The first quarter displays materials with positive permittivity and permeability, and they are known as righthanded materials. This category includes dielectric materials. In the second quarter, the permittivity is negative, but the permeability is positive. This category includes metals and plasmas; plasma materials exhibit identical features within certain frequency ranges. In addition, these materials are also known as Epsilon-negative materials. The fourth quarter is characterized by negative permeability and positive permittivity. This category includes gyrotropic magnetic materials. The negative sign of μ indicates that the direction of the electric and magnetic fields is opposite to the direction of the incident EM-wave. Furthermore, the materials in the second and fourth quadrants, when one of the two values is negative and the index of refraction becomes totally imaginary, cannot support propagating waves. As suggested by Veselago, the third quarter exhibits a double-negative sign of material or left-hand material (Kotsuka, 2019). Materials have a negative refractive index due to their double-negative characteristics. This is a special feature absent in natural materials.

According to the previous description, MMs are manufactured in laboratory, effectively homogeneous as the

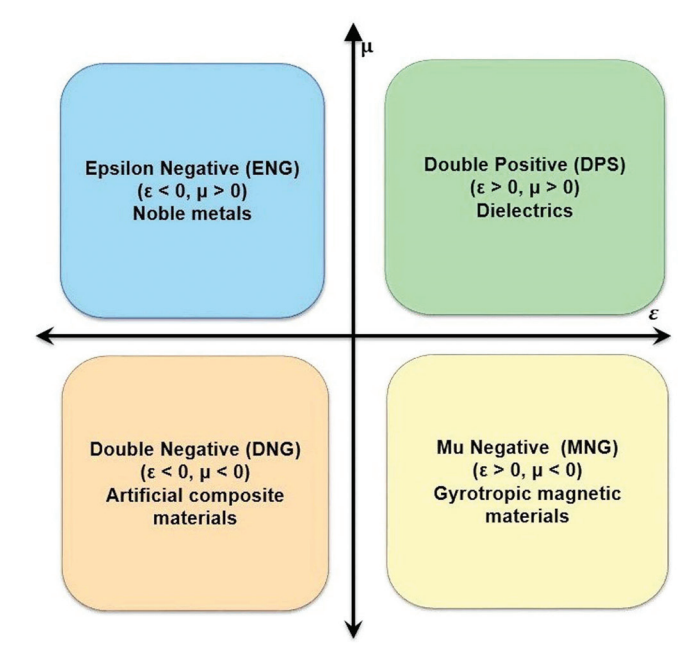


Fig. 1. Materials classification based on permeability and permittivity (Ziolkowski, 2006).

component size less than $\lambda/4$ of the incident wave and exhibit quite uncommon characteristics such as $\epsilon < 0$ and $\mu < 0$.

III. MMA

A MMA is a device made of an engineered material with a periodic array structure at a sub-wavelength scale. It possesses optical features unavailable in traditional natural optical materials. This kind of structure possesses the capability to absorb electromagnetic waves, thereby reducing transmission, reflection, and scattering to zero percent. Afterward, it transforms into various forms, such as heat or electricity. An MMA typically consists of a periodic top metallic pattern, a dielectric spacer layer, and a continuous metallic plate at the bottom (Duan, et al., 2018). In MM prefect absorber (MMPA) design, the first patterned layer is crucial because it lets the impedance match the environment, which means there is zero reflection at resonance frequencies. The second dielectric layer spreads out the electromagnetic energy inside the absorber cavity. The metallic ground layer effectively blocks all incident electromagnetic waves. There are two types of absorption mechanisms: dielectric loss and Ohmic loss (Tuong, et al., 2013). The dielectric loss is a dispersion of electromagnetic wave energy that takes place inside a dielectric material and the ohmic loss is the loss of electrical energy caused by the resistance in a circuit as current passes through it. To move beyond the structure and its function, the next section introduces the theoretical foundation that explains how MMA achieves such kind of absorption.

IV. THEORETICAL FOUNDATIONS OF MMAS

Several theoretical approaches have been developed to explain the MMA absorption, each focusing on a different physical mechanism, such models that maximize absorptions and minimize the reflection and transmutation to zero (impedance matching) or an interference model to explain the absorption in the MM cavity. Alternatively, the Effective Medium Model treats MM as a homogeneous medium with effective properties, while the Equivalent Circuit Theory treats MM as an electrical circuit element. Furthermore, the same basic idea can be applied to both narrowband and broadband.

A. Impedance Matching Theory

Impedance matching is a key requirement for achieving perfect absorption. Typically, MMAs consist of three layers arranged in a specific structure: The conventional metal-dielectric-metal configuration, which is composed of a top metal resonator, an intermediate dielectric layer, and a ground metal reflector. The relationship between absorption, transmission, and reflection can be represented as (Liu, et al., 2023).

$$A_{bc}(\omega) = 1 - T_{ra}(\omega) - R_{ef}(\omega)$$
 (2)

The thickness of the ground material is significantly larger than the skin depth (the depth to which an electromagnetic wave penetrates a material before its amplitude decreases to 1/e (approximately 37% of its surface value), which prevents the transmission of light waves. This metal completely blocks the transfer of light waves, T_{ra} . (ω) = 0. The Fresnel equations allow us to mathematically represent the reflectivity (R_{ef}) at normal incidence (i.e., angle of incidence $\theta = 0^{\circ}$).

$$R_{ef}(\omega) = \frac{Z_{MMA} - Z_0^2}{Z_{MMA} + Z_0} = \frac{\sqrt{\mu_r} - \sqrt{\varepsilon_r}^2}{\sqrt{\mu_r} + \sqrt{\varepsilon_r}}$$
(3)

Where the impedance of free space $Z_0 = \sqrt{\frac{\varepsilon_0}{\mu_0}}$ is equal to 377 Ohm, and the impedance of the MMA is represented by $Z_{MMA} = \sqrt{\frac{\varepsilon_r}{\mu_r}}$. By subtracting equation (3) from (2), the absorbance is determined as follows (Zhu, 2018, Verma and Meena, 2023).

$$A_{bs}.(\omega) = 1 - \frac{Z_{MMA} - Z_0^2}{Z_{MMA} + Z_0^2} = 1 - \frac{\sqrt{\mu_r} - \sqrt{\varepsilon_r}^2}{\sqrt{\mu_r} + \sqrt{\varepsilon_r}}$$
(4)

The previous equation shows that when the impedance matching condition ($Z_{\text{MMA}} = Z_0$ or $\mu_{\text{r}} = \epsilon_{\text{r}}$) is achieved, perfect absorption can be obtained. Landy, et al. demonstrated that the MMA can achieve perfect absorption when both electric and magnetic components are present (Landy, et al., 2009). Impedance matching is possible with $Z_{\text{MMA}} = Z_0$, but if only one component is present, impedance matching is not possible with $Z_{\text{MMA}} > Z0$.

B. Effective Medium Theory

Because of their unique structures, MMs made from two or more composite materials should be homogeneous for perfect incident EM wave transmission. This is why EMA, or "effective medium theory," is essential for the first layer (MM layer) of MMPA, which can generate an electromagnetic response. At the interface between various components, the EM characteristics are typically discontinuous. On the other hand, the incident wavelength is longer than the unit cell sizes of the MM. We can assume that the MM as a whole (its effective medium) and its properties determine its parameters in terms of frequency-dependent complex effective permittivity ($\epsilon_{\rm eff}$ (ω)) and effective permeability ($\mu_{\rm eff}$ (ω)). Hence, the effective impedance can be expressed by (Liu, et al., 2023).

$$Z_{eff.} = \sqrt{\frac{\mu_{eff.}}{\varepsilon_{eff.}}} Z_0 \tag{5}$$

Furthermore, the effective permittivity and effective permeability are given by (Koschny, et al., 2004, Smith, et al., 2000, Fu and Cui, 2019).

$$\varepsilon_{\text{eff.}}(\omega) = 1 - \frac{\omega_{plasma}^2}{\omega^2 + j\omega\gamma} \tag{6}$$

ARO p-ISSN: 2410-9355, e-ISSN: 2307-549X

$$\mu_{\text{eff.}}(\omega) = 1 - \frac{F\omega^2}{\omega^2 - \omega_0^2 + j\omega\gamma} \tag{7}$$

Where $\omega_{\textit{Plasma}}$, ω , and ω_0 are plasma frequency, angular frequency of the incident wave, and oscillation frequency, respectively. This is where F represents the area ratio of the Split-Ring Resonator (SRR) into unit cell size and γ is the damping frequency, an SRR. This is a type of resonator shaped like a ring with narrow gab, which is commonly used in MMs, as shown in Fig. 2. In materials with large electromagnetic wave loss, the imaginary components of $\varepsilon_{\textit{eff}}$ and $\mu_{\textit{eff}}$ are significant. When impedance matching and high loss take place simultaneously, MMs can achieve a perfect absorption. The effective medium model intuitively explains the achievement of perfect absorption.

C. Interference Theory

Interference theory (Chen, 2012) is widely used to explain absorption features of MMAs. This is a model which is based on interferences, describing how multiple reflections of the incident wave occur between the top metal resonator and bottom metal plate. This model assumes an infinitesimal impedance surface for the top MM layer, as can be seen in Fig. 3 (Duan, et al., 2019). When electromagnetic waves hit the air-metal interface, they reflect and transmit with a reflection coefficient $\tilde{R}_{12} = R_{12}e^{i\theta_{12}}$ and transmission coefficient $\tilde{T}_{12} = T_{12}e^{i\theta_{12}}$. The transmitted wave keeps on moving through the spacer layer until it hits the ground plane with a propagation wave number $\tilde{\beta} = \beta_{Phase} + i\beta_{Substrate} = \sqrt{\varepsilon_d k_0 d}$, where β_{Phase} represents propagation phase, $\beta_{Substrate}$ represents substrate absorption, ε_d is permittivity of dielectric material, d is the thickness of the substrate, and k_0 is the free space wave number.

Following the reflection off the ground plane and the incorporation of an additional propagation phase, $\tilde{\beta}$ there is a subsequent partial reflection and transmission at the airspacer boundary involving cross-resonators. These processes

are characterized by the coefficients $\tilde{R}_{21} = R_{21}e^{i\Theta_{21}}$, $\tilde{T}_{21} = T_{21}e^{i\Theta_{21}}$ then the combination of the multiple reflections gives (Chen, 2012, Duan, et al., 2019):

$$R = R_{12} - \frac{T_{12} T_{21}}{\left\{ R_{21} + e^{(-2i\beta)} \right\}}$$
 (8)

Where $\beta = n_s k_0 d$ represents the one-way phase delay in the spacer, and n_s is the refractive index of the spacer material.

The first term depicts the direct reflection from the cross-resonator array, whereas the second term is the direct result of the superposition of multiple reflections between the cross-resonator array and the ground plane. The absorption is subsequently obtained by A_{bs} . $(\omega) = 1-R_{ef}$. (ω) , due to the transmission coefficient being zero. Hence, the interference theory explores the reflection and transmission mechanisms of a cavity.

D. The Equivalent Circuit Theory

The equivalent circuit is a common and effective technique to comprehend the operation of an electromagnetic-wave absorber. To accomplish this goal, the transmission line theory (TLT) is used to provide a comprehension of the structure in question. Furthermore, research has shown that LC circuits are an effective way to describe the behavior of resonant absorbers. The number of resonances that are presented by the absorber is directly related to the number of lumped elements that are employed in these equivalent circuits. As an illustration, a single resonant absorber will only provide a single-series RLC that is connected in parallel with the grounded dielectric. Fig. 4 illustrates a typical equivalent circuit for a metal-backed absorber (Aliqab, Armghan and Alsharari, 2024).

The mathematical description of the impedance of the lossy FSS is (Aliqab, Armghan and Alsharari, 2024):

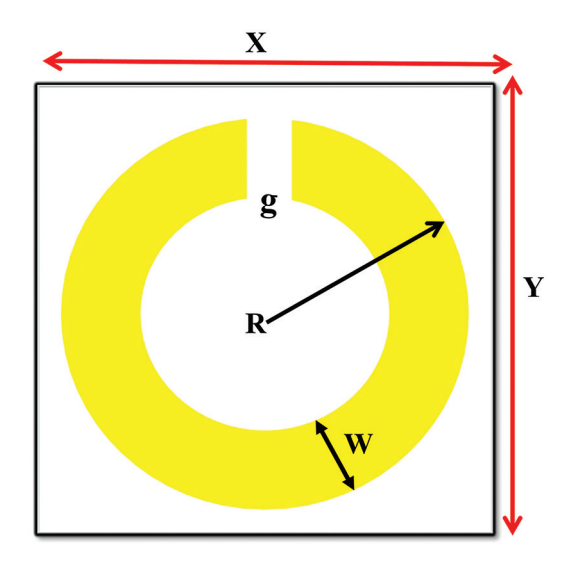


Fig. 2. A split-ring resonator (SRR). F is the ratio of the SRR area to the unit cell area.

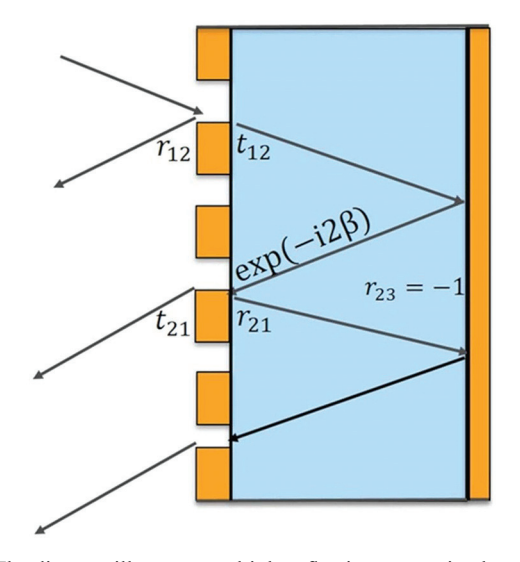


Fig. 3. The diagram illustrates multiple reflections occurring between the ground plane and the metamaterial layer.

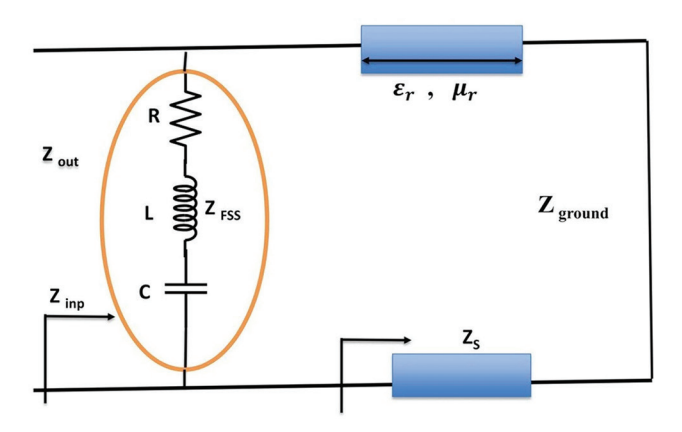


Fig. 4. Illustrates the equivalent circuit of absorber ZFSS unit cell.

$$Z_{FSS} = R - j \left(\frac{1 - \omega^2 LC}{\omega C} \right) \tag{9}$$

Further, Z_{input} represents the parallel connection between Z_{FSS} and the impedance of the dielectric spacer Z_d , which is given by (Choukri, et al.; Ghosh and Srivastava, 2014):

$$Z_{input} = \frac{Z_d Z_{FSS}}{Z_d + Z_{FSS}} \tag{10}$$

$$Z_{d} = i\sqrt{\frac{\mu_{rd} \mu_{0}}{\varepsilon_{rd} \varepsilon_{0}}} \tan(\beta_{d}, h) = iZ_{c} \tan(\beta_{d}, h)$$
(11)

Here, $\beta_d = \frac{\beta_0}{\sqrt{\varepsilon_{rd}\mu_{rd}}}$ is the propagation constant within the

substrate. Furthermore, ε_{rd} and μ_{rd} represent the constitutive parameters of the substrate and Z_c denotes its characteristic impedance of the substrate. The reflectivity coefficient of this absorber is given by (Huang, et al., 2015):

$$R_{ef.} = \frac{Z_{input} - Z_0}{Z_{input} + Z_0} \tag{12}$$

The absorption coefficient is given by:

$$A_{bs.} = 1 - R_{ef.} = 1 - \frac{Z_{input} - Z_0}{Z_{input} + Z_0}$$
(13)

Perfect absorption happens when impedance matching is satisfied (Z_{input} Z_0 = resulting in R_{ef} = 0).

V. Broadband MMA (BMMA)

Typically, MMAs, including MM perfect absorbers (MMPA), are classified based on the bandwidth of EM frequencies they can absorb whether it is narrow or broad. The narrowband can be further categorized into single band (Landy, et al., 2009, Liu, et al., 2010) dual band (Wen et al., 2009, Tak, Jin and Choi, 2016), triple band (Wang, et al., 2018, Wang, et al., 2021), and more multifrequency bands (Moniruzzaman, et al., 2020, Wang,

2016, Wang and Wang, 2015). BMMAs are capable of absorbing electromagnetic radiation across a broad spectrum of frequencies. This makes them ideal for applications requiring broad-spectrum absorption, such as solar energy harvesting, stealth technology, and military applications. However, achieving BMMA in high frequencies compared to the radio and microwaves, such as IR or visible region, still poses a challenge. This challenge arises from the unit cell size of patterned array structures. In the sub-wavelength condition, the unit cell size must be significantly smaller than the incident EM wave wavelength. Since IR and optical EM waves have wavelengths of a few hundred nm, the patterned array should have a periodicity of 100 or a few tens of nm. Current nanofabrication techniques can handle the entire range of unit-cell sizes. Despite this, combining individuals within a single cell remains a significant challenge. Moreover, MMs can achieve broadband absorption through a variety of methods. This includes combining multi-resonant cells and integrating them through a coplanar configuration (Chen, et al., 2009) (Kim, et al., 2015, Wen, et al., 2013) and using a multi-layered architecture with vertical arrangement (Zhu, et al., 2014, Yang Shen, et al., 2015). Furthermore, it can be obtained by the integration of electrical components (Zhang, et al., 2018, Al-Badri, 2020) or by nanostructures (Lin, et al., 2017).

VI. CHARACTERISTICS OF BMMAS

A. Polarization Independence

Polarization independence in BMMAs is the ability of an MMA to absorb electromagnetic waves at the same rate (Zheng, et al., 2023), regardless of the polarization state of the incoming light. This property is suitable for practical applications, such as in solar energy harvesting, radar technology, and thermal detection where the orientation varies. They can outperform traditional MMAs in terms of performance and dependability. These absorbers are designed to demonstrate the same absorption characteristics for both transverse-electric mode (TE) and transverse-magnetic mode (TM) of electromagnetic radiation. For example, an extremely thin BMMA made up of four lumped resistors shows absorption levels higher than 90% across a wide frequency range, from 14.35 to 29.18 GHz (Saadeldin, et al., 2023). It was seen that the structure exhibited a significant absorption over incoming angles ranging from 0° to 50°. In another work (Chowdhury, et al., 2022), an ultra-BMMA showed consistent polarization in both electric and magnetic modes in the visible range from 400 to 750 nm, as shown in Fig. 5. The absorber maintains stable performance even at oblique incoming angles up to 60. The absorber demonstrates stability at broader angles of incidence, indicating its suitability for various polarizations and angles. Achieving polarization independence involves design choices and precise fabrication methods. This can be effectively achieved by incorporating structural symmetry (Lee, et al., 2016), multi-resonant elements (Jang, et al., 2014), and similar techniques.

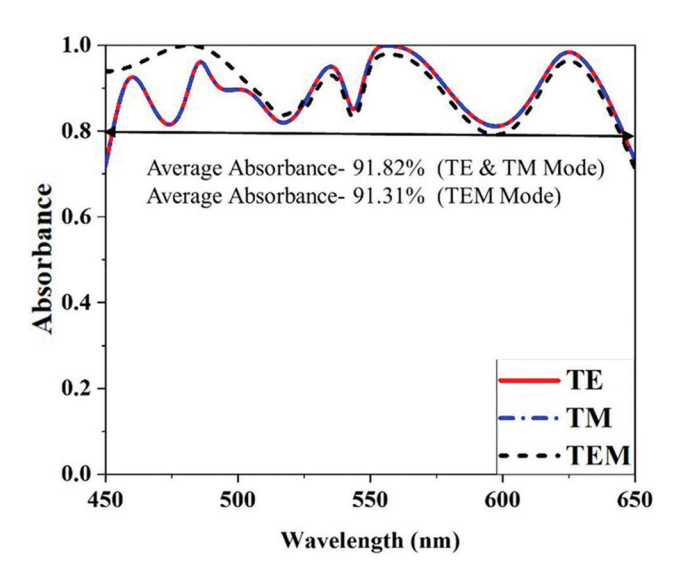


Fig. 5. Comparison of absorbance properties under transverse-electric, transverse-magnetic, and transverse electromagnetic polarized modes (Chowdhury, et al., 2022).

B. Broad Angle

BMMAs with a wide incident angle have been engineered to tackle the issue of attaining high absorption rates across a broad range of incident angles. Those engineered structures can attain significant absorption even when the angle of incidence of electromagnetic waves diverges widely from the normal direction. This reduction is due to the nonlinear relationship between reflection coefficient and the incidence angle for both TE and TM. In a theoretical work (Jiao, et al., 2021), it has been shown that when the incident angle rises from 0^{0} to 60^{0} , throughout the operational bandwidth, the average absorption for TE-polarized light exceeds 94%, while for TM-polarized mode, it remains above 93%, as shown in Fig. 6. This divergence underscores the challenge of achieving optimal absorption across a range of angles and polarization states. The wide-angle MMAs offer numerous advantages compared to traditional absorbers. Their capacity to exhibit significant absorption across a wide range of incoming angles makes them perfect for many applications where incident waves come from multiple directions. The integration of wideangle capabilities with BMMAs enhances their functionality in a wide range of applications, such as defense technologies (Wang, et al., 2019) and energy harvesting (Hoa, et al., 2019). A combination of the abilities of wide-angle and broadband will not only broaden the operational bandwidth but also be an important factor in future technologies.

VII. BMMAs with Different Architectures

BMMAs are categorized into varied types based on the architectural design (Yu, et al., 2019, Wang, et al., 2023a). This review focuses on the major types of these absorbers.

A. Planar Broadband Absorbers

On a single flat plane, the horizontal stacking method allows for the placement of multiple resonant components of the same size or different sizes, side by side in the unit cell (xy-plane). These resonators are designed to target several frequencies that partially overlap with each other. The combination of two separate resonators of unit cell is a method for achieving a planer broadband absorber. Researchers (Gandhi, Babu and Senthilnathan, 2021) proposed a design consisting of two resonators, each exhibiting its own specific absorption wavelength, as shown in Fig. 7a and b. The inner resonator exhibited a higher absorption efficiency, capturing approximately 50% of the incident energy compared to the outer resonator which absorbs about 18%. When both resonators were combined in the unit cell, the absorption efficiency was increased significantly. The combination of resonators resulted in overlapping 90% of the bandwidth between 2.54 and 5.54 THz. Fig. 7c shows the absorption of two independent resonators, separately, while Fig. 7d shows how the combination of two resonators has created a broadband absorption. Finally, the design structure shows that the absorber is polarization-insensitive and maintains 90% effectiveness up to 40° of incident angles.

An alternative approach to building a planar broadband absorber with multiple resonators is the fabricated design described in (Liu, et al., 2012b). This design makes use of a dielectric layer to separate a number of circular metal patches of varied sizes from a ground metal plate. By manipulating the size and arrangement of these patches, the design creates closely spaced resonance frequencies, enabling broadband absorption. Furthermore, the proposed design demonstrates insensitive polarization and incident angle, maintaining effective absorption across a wide range of angles (0°–60°). In addition, there is a strong agreement between the experimental measurements and theoretical predictions at incident angles of 10°, 30°, and 60°.

The square metallic ring is a structure that is commonly used in the applications of multiband MMAs. In 2015, researchers (Wang, et al., 2014) proposed an absorber capable of achieving four absorption peaks using this configuration. According to the literature (Shen, et al., 2018), the broadband design consists of four-square metallic rings and a metallic ground plane, which are separated by a dielectric layer. For each sub-unit cell in the top metallic pattern, there are four varying-sized square metallic rings. They further refined the design by modifying the neighboring resonance peaks of each sub-cell, merging them to overcome the narrowband limitation and effectively generate broadband absorption. In another work (Cai, et al., 2024), a theoretical approach was presented in the visible and near infrared (IR) region, considering all dielectric materials such as gallium arsine (GaAs). The concept was to design an ultra-broadband, wide-angle plasmonic light absorber (PLA), and metasurface absorbers that consist of two-dimensional structures. A tungsten (W) substrate was utilized to support a single periodic array of the attached GaAs cylinder resonators. The design achieved over 90% of absorption across the range from 390 to 2090 nm. The equivalent circuit model (ECM) further illustrates the remarkable ultrabroadband strong absorption that the suggested PLA displays. The results of the fullwave numerical simulation using the finite element method

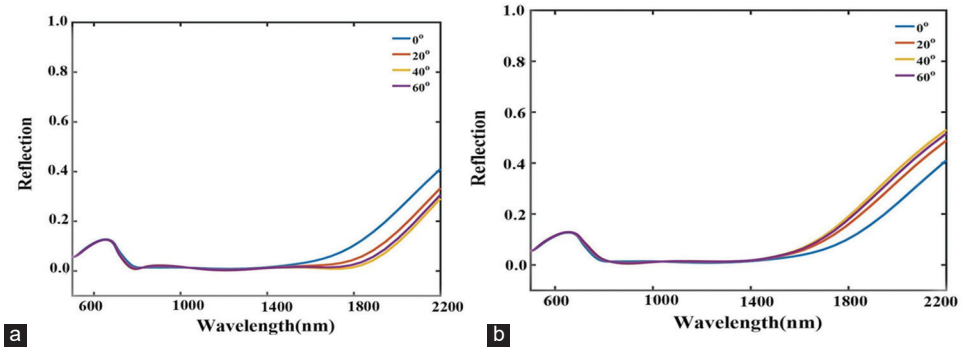


Fig. 6. Impact of oblique incoming light on the reflectance spectrum: (a) transverse-electric-polarized mode and (b) transverse-magnetic-polarized mode (Jiao, et al., 2021).

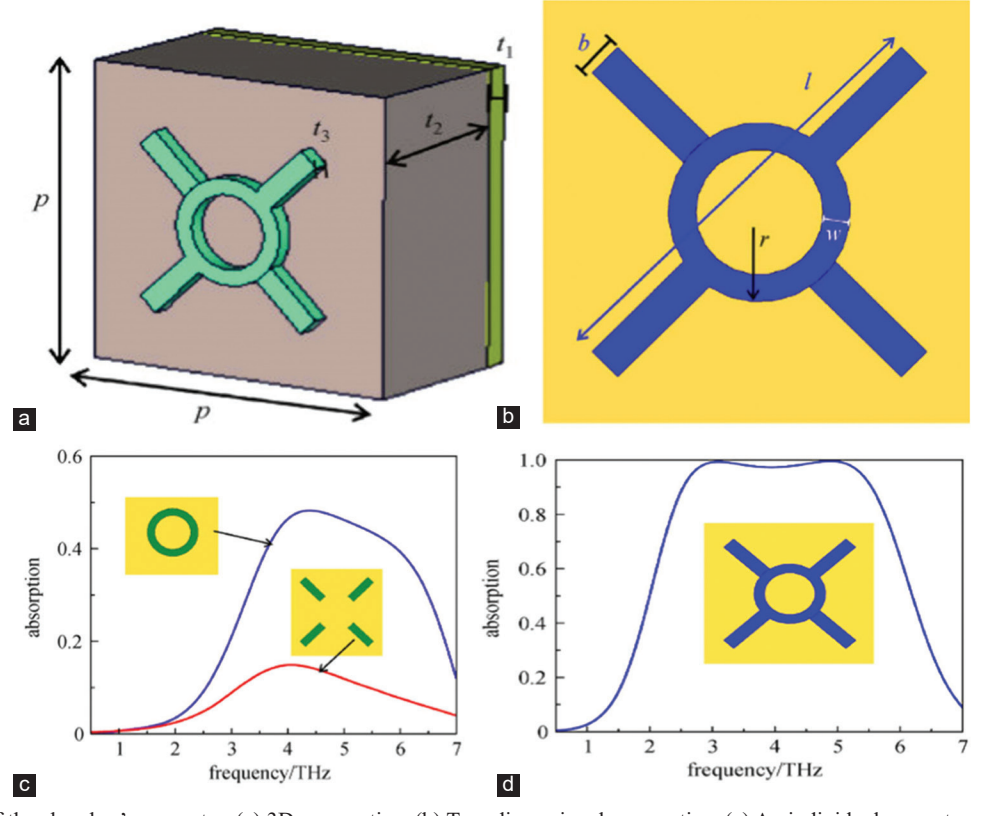


Fig. 7. Design of the absorber's geometry, (a) 3D perspective, (b) Two-dimensional perspective, (c) An individual resonator, and (d) Combined resonators (Gandhi, Babu and Senthilnathan, 2021).

(FEM) showed excellent agreement with their work. GaAsbased metasurfaces enable the absorption of a broad range of frequencies through multiple resonances, such as excited propagating surface plasmon (PSP), located surface plasmon (LSP), and cavity resonance modes, while maintaining costeffectiveness without the need for noble metals. The absorber is polarization-insensitive and consistently performs across a wide incident angle, making it ideal for use in thermal imaging, photodetectors, and solar energy harvesting.

B. Vertical Broadband Absorbers

Planar BMMAs are facing significant challenges due to two common factors (Padilla and Fan, 2022, Yu, et al., 2019). One factor is the strong interaction between subcellular

resonators. This mutual interaction leads to a decrease in the oscillation strength. This interaction reduces broadband absorption capacity, resulting in a decrease in absorption intensity. The size of the super-unit cell and the restriction of the subunit cell cause structural limitations, which in turn reduce the filling factor of the super-unit cell. The researchers attempt to address this issue by arranging the resonators vertically to be able to broaden their absorption range in this way. In the vertical planes, stacking additional resonant layers interspersed with shorter intervals can improve absorption. It allows for an increase in the operational bandwidth.

The authors in (Ye, Jin and He, 2010) elaborated on how their design achieved a broadband absorption by stacking multilayers in vertical directions with different geometrical sizes. Herein, each layer consists of a metallic gold cross and lossy polymer as the separation layer (Fig. 8a). The three layers are arranged vertically in such a way that the size will increase gradually from the top to the bottom layer. Each layer has a different resonance frequency due to varying wire length. This results in numerous resonance peaks, thereby forming a broadband absorption, as shown in Fig. 8b-d. To further understand the resonance behavior, a simpler LC model has been introduced. Numerical simulation indicated three absorptivity peaks at frequencies of 4.55, 4.96, and 5.37 THz, as shown in Fig. 8d. This three-layer arrangement achieved a 1.03 THz frequency band with nearly perfect absorption >97%, whereas the full width at half maximum of the absorption rises to 1.9 THz, reflecting approximately 38% of the center frequency.

A broadband design capable of operating from ultraviolet (UV) to the long wave IR (LWIR) regions based on the CMOS-compatible materials was proposed by (Yue, et al., 2020). The design draws inspiration from multilayered structures that employ resonant patches of different sizes to achieve ultra-broadband absorbers. More precisely, the absorber consists of a multi-layered sawtooth of twenty alternating layers of aluminum (Al) and zinc sulfide (ZnS), as shown in Fig. 9a. The structure was carefully designed for optical and plasmonic characteristics across the wavelength

range, as shown in Fig. 9b. The ultra-broadband absorber's performance depends on layering metal/dielectric material, which creates overlapping resonance wavelengths across the spectrum. High frequencies are absorbed by upper layers (Fig. 9c), while low frequencies are capable of penetrating the upper layer so that they are absorbed at the lower one (Fig. 9d). This process of cascading absorption will be very efficient over a wide range of wavelengths. A pyramid-like structure in the sawtooth absorber provides polarization-insensitive absorption under normal incidence and 90% of absorption up to 50° of incidence angle. The structure maintains a relatively modest total thickness compared to the operating wavelengths, facilitating simple integration with current technology.

Alternating metal-dielectric materials arrangement in a vertical direction was approached to form a broadband absorber. Alternating metals, two different dielectric materials, is a significant step toward achieving a broadband absorber. Other researchers (Chen, et al., 2024) proposed a design that combines eight layers of titanium (Ti) and two dielectric materials, silicon dioxide (SiO₂), and aluminum oxide (AlO₃), to form pyramid-like structures. From bottom to top of the structure, the titanium is placed in odd layers, while SiO₂ is in layers 2 and 7, and AlO₃ is put into the layers 5 and 8. This is designed to maximize absorptivity across a broad spectrum,

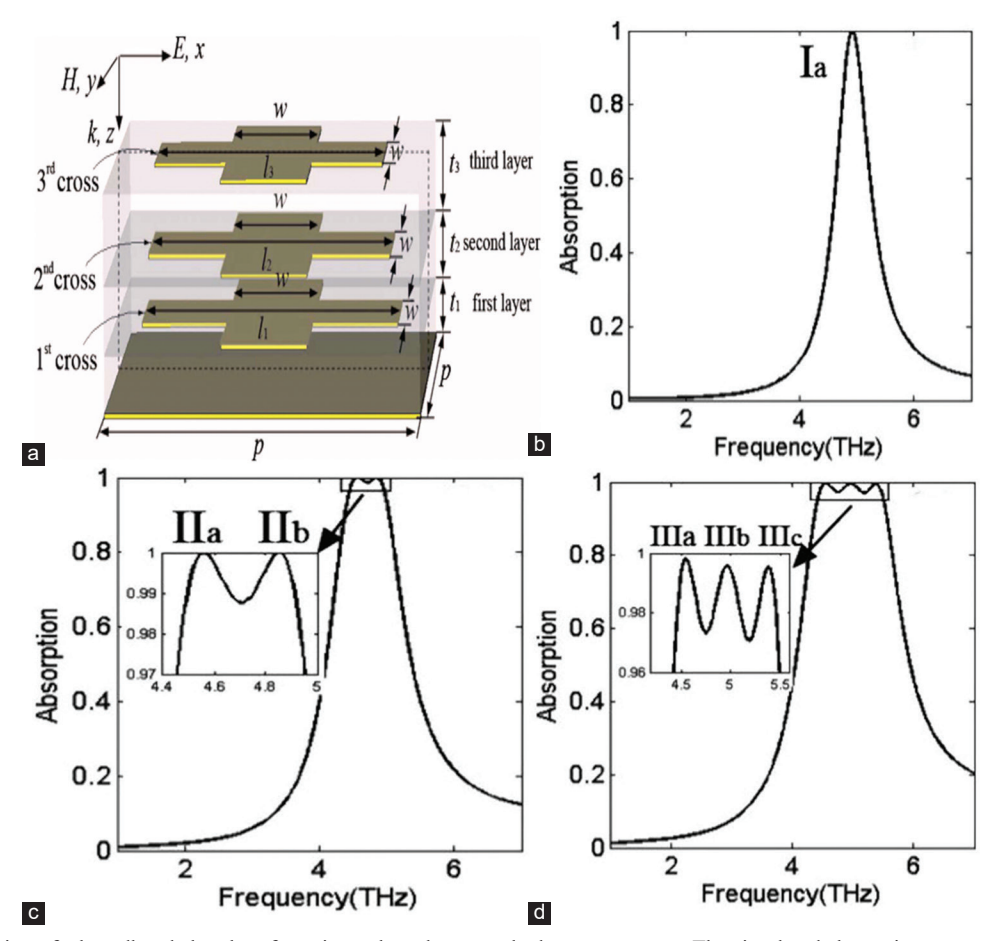


Fig. 8. (a) The design of a broadband absorber, featuring a three-layer stacked cross structure. The simulated absorption spectra of this structure are presented in (b), (c), and (d) (Ye, Jin and He, 2010).

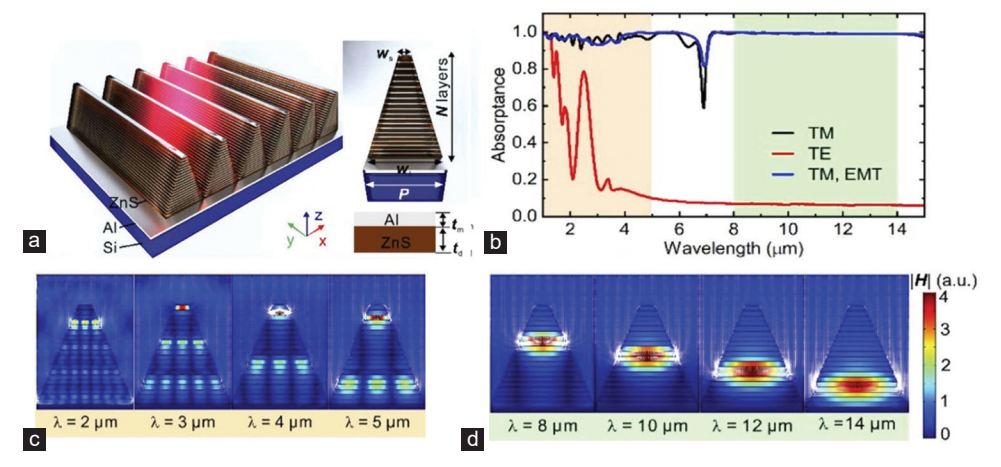


Fig. 9. (a) Diagrammatic representation of the saw-toothed metamaterial absorber, (b) The corresponding absorption spectrum depicts the incidence of transverse-magnetic-polarized light in black and transverse-electric-polarized light in red, (c) Magnetic field distributions (illustrated as surface plots) and Poynting vectors (indicated by white arrows) of absorber at characteristic wavelengths within the short-wave infrared and mid-wave infrared bands, and (d) It is similar to (c), but for wavelengths in the long wave infrared band (Yue, et al., 2020).

ranging from UV A (335 nm) to middle IR (4865 nm). The study utilized COMSOL multiphysic simulations to optimize the absorber's structure, aiming at achieving absorptivity of greater than 90% across the targeted wavelength range. This design has various advantages. First, the design incorporates an absorber metal/two-dielectric arrangement that leverages the unique properties of each material. The arrangement enhances absorbance through multiple modes of resonances, such as surface plasmon resonance and the interference effect. Furthermore, it maintains a structure that is both practical and simple to manufacture. Finally, this method makes the absorber efficient across a wide spectrum, making it appropriate for many optical applications.

C. Broadband MMs Incorporating Lumped Elements

Broadband MMs have traditionally been high-tech manmade composites that can absorb electromagnetic waves across a broad spectrum, from microwaves to the visible light spectrum. However, those absorbers are large, bulky, and complex to fabricate at increasing costs (Aalizadeh, et al., 2018). In this approach, the bandwidth is extended by adding layers into the structure. One alternative is to use a broadband absorber with lumped elements, which involves arranging resistors, capacitors, and other lumped element circuit components in a metallic pattern within unit cells. For the creation of broad MMAs, a new way has been found to combine the transmutation line method with a reduction

Q-factor that is calculated by $Q_F = \frac{1}{R} \sqrt{\frac{L}{C}}$. This strategy involves combining composite elements into BMMA, enhancing their ability to absorb a wide range of frequencies effectively.

In a research work (Nguyen, et al., 2020), a numerical study on the design of BMMAs was reported by using split circle rings (SCR) and lumped resistors for X-band applications. The structure is composed of a top layer of copper (Cu), with a ground layer separated by a dielectric layer (FR-4).

This dielectric material is a typical printed circuit board (PCB) substrate, which is composed of fiberglass-reinforced epoxy laminate, and its relative permittivity is about 4.4. Fig. 10a shows the proposed design, while the corresponding equivalent circuit diagram with lumped resistors is shown in Fig. 10b. The results demonstrate that the addition of four lumped resistors enables the absorber to achieve broadband absorption with high absorptivity, achieving over 90% across the frequency range of 7.8–12.6 GHz. The outcome shows that lumped resistors are an important method for broad absorption because they enable impedance matching and well-competition multi-absorption peaks (Fig. 10c). The structure exhibits absorptivity that exceeds 70% in the frequency range of 6.8–11.8 GHz, with wide incidence angles ranging from 0° to 30° for both TE and TM polarizations.

Theoretical and practical approach for designing broadband MMs that effectively operated across the S, C, and X bands in microwave regions presented by (Zhang, et al., 2023). The unit cell consists of FR-4 as a dielectric spacer, while the top pattern and back reflector are made from copper (Cu). The process of brooding absorption consists of four stages. The first stage displays a narrow band around 15 GHz. Furthermore, to achieve absorbance over 90% between 14 GHz and 15 GHz and perfect absorption of over 99% at 14.6 GHz, eight resistors are added to the design. An air layer is added between the dielectric spacer and ground metal plate to decrease the relative permittivity, enabling the broaden bandwidth to be extended beyond what was obtained in the second stage. This slows down the rate at which electromagnetic waves propagate through the material, thereby altering the resonance frequency and enhancing absorbance. In the final stage, optimization was carried out on the lump resistance and substrate height for achieving a broadband across the S, C, and X bands with absorption over 90% from 2.7 GHz to 12.7 GHz, resulting in a relative absorption bandwidth of 130%. The absorber was theoretically based on transmission line theory, with an ECM providing a methodological explanation through impact

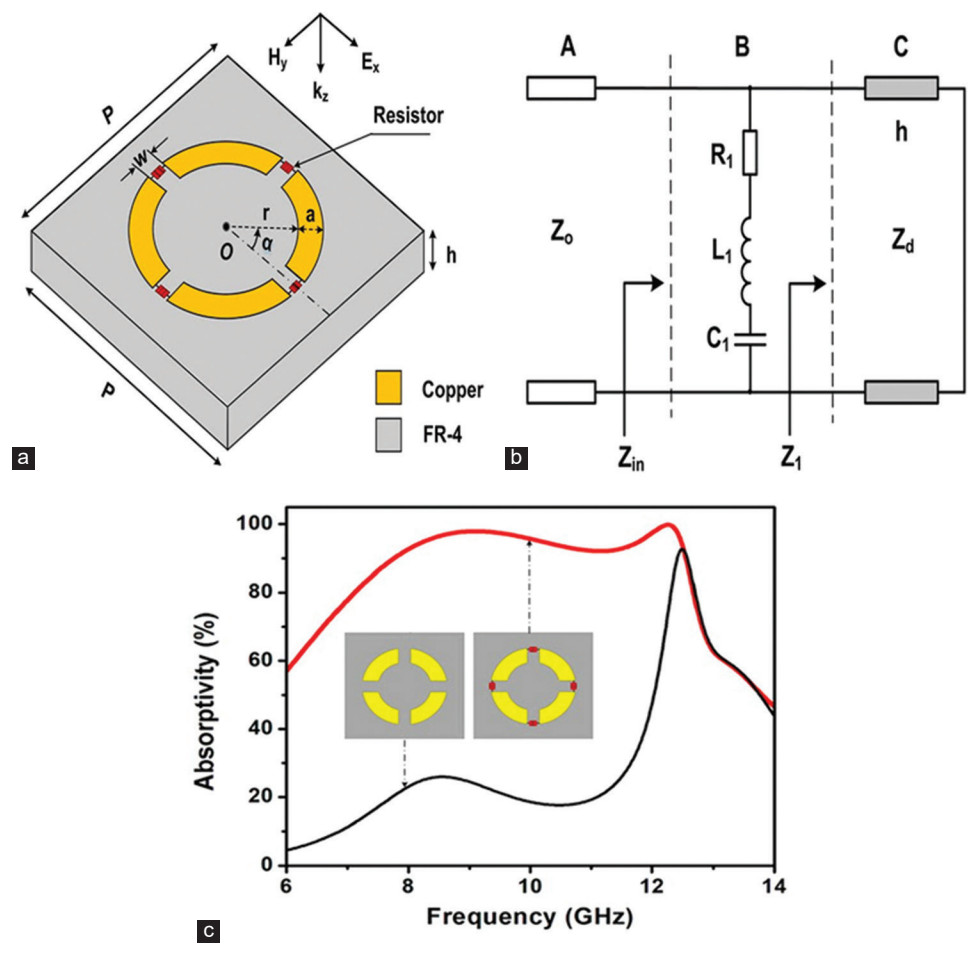


Fig. 10. Schematic representation of the proposed metamaterial absorber's unit cell: (a) Three-dimensional view, (b) Corresponding equivalent circuit diagram, and (c) Absorption spectra of the designed metamaterial absorber structures, comparing configurations with and without lumped resistors, when subjected to normal incidence for transverse-electric polarization (Nguyen, et al., 2020).

matching and design parameter optimization. Furthermore, experimental results confirm the theoretical predictions, as the fabricated absorber exhibits excellent absorption in the desired frequency range.

For microwave broadband MM absorption, a structure consisting of lumped resistors and a double frequencyselective surface (FSS) layer has been successfully demonstrated by (Xie, 2023). The two FSS layers are separated by an air gap, with lumped resistors strategically placed to interact with each gab space (Fig. 11a-d). This combination of FSS layers and resistors significantly enhances the absorber's broadband performance. The value of the resistors plays a crucial role in determining the efficiency of absorption. Lower resistance values are insufficient to absorb electromagnetic waves effectively, while higher resistance values can degrade performance at higher frequency bands. The upper layer of lumped resistors is particularly important, contributing to enhanced absorption by adding an extra layer of attenuation. Through analysis, the optimal value for the top lumped resistor was found to be $R_1 = 100$ ohm, which resulted in an absorption rate exceeding 98% across the 8.41–20.98 GHz range. Increasing the resistance to 160 ohms maintained similar performance but with a slightly narrower

bandwidth (Fig. 11e). The bottom resistor's role is to balance absorption and bandwidth effectively, as shown in Fig. 11f. Key parameters, including the height of the dielectric layer, the air gap, and the resistor values, were optimized to maximize the absorber's performance. Numerical simulations conducted using CST Studio Suite 2020 confirmed that the absorber consistently achieves over 98% absorption across specific frequency ranges. Furthermore, the absorber maintained high efficiency at oblique incidence angles up to 30°, demonstrating impressive angular stability.

D. BMMA with Plasmonic Nanostructure

Metals such as gold and silver typically form plasmonic nanostructures, from which artificial structures smaller than the wavelength of visible light can be fabricated. They also exhibit plasmon oscillation of the conduction band electron in response to external radiation, resulting in improved light absorption and scattering. This is achieved through a phenomenon known as LSP resonance (LSPR). The integration between plasmonic nanostructures and MMAs is another approach to achieving broadband absorption. This process enables the absorber to combine multi-peak resonance, additionally allowing it to capture light across a

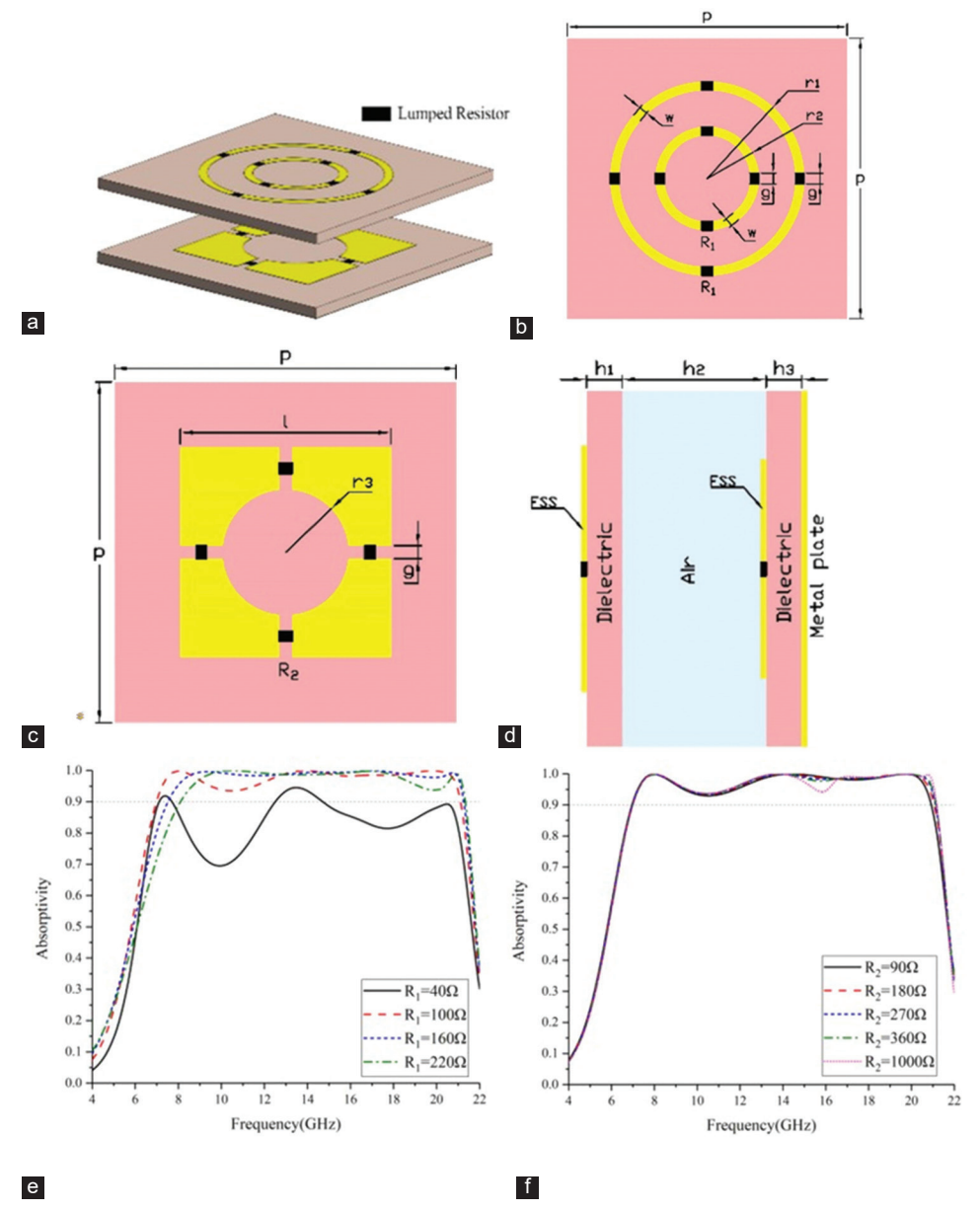


Fig. 11. The configuration of the proposed absorber and its design specifications. (a) A 3D perspective of the absorber's unit cell, (b) The unit cell structure of the absorber's top layer, (c) The unit cell design for the bottom layer of the absorber, (d) A side view illustration of the absorber's unit cell, (e) Absorptivity for different resistor values in the top layer, and (f) Absorptivity for different resistor values in the bottom layer (Xie, 2023).

wide range of frequencies, from visible to IR. Because of their tunable geometry, plasmonic nanostructures are capable of effectively absorbing light at multiple wavelengths and are generally independent of the polarization or of the angle of incoming light, making them essential for solar energy harvesting and optical sensors.

A BMMA for visible spectrum (400–800 nm) designed using manganese-Silica-manganese (Mn-SiO₂-Mn) structure optimized by (Sayed, et al., 2023). The upper layer (Mn) consists of a square disk encircled by a square ring-shaped manganese structure, functioning as a resonator, and SiO₂ as a dielectric material. This serves to separate the top resonator from the ground plate layer (Mn), as shown in Fig. 12a. The authors successfully designed an MMA with nearly perfect absorption in a cross-visible spectrum. The

absorber achieved absorption over 98.72% for 400–800 nm and 99% for 447–717 nm, with an ultra-wide bandwidth of 270 nm (Fig. 12b). The geometrical parameters of the proposed absorber have been optimized using the Particle Swarm Optimization algorithms to fine-tune the geometrical parameters of the unit cell, considering the designs shown in Fig. 12c. Fig. 12d illustrates the strong interaction of light with the inner square disk and the outer square ring. The proposed structure absorption, compared to the planar structure (first stage of design), indicates a strong absorption. This is also linked to the presence of Surface Plasmon Polaritons, LSPR, and PSP modes within the Mn-based structure. The absorber retains more than 85% efficiency at incident angles up to 70° for both TE and TM polarizations, making it ideal for applications like sensors and solar energy

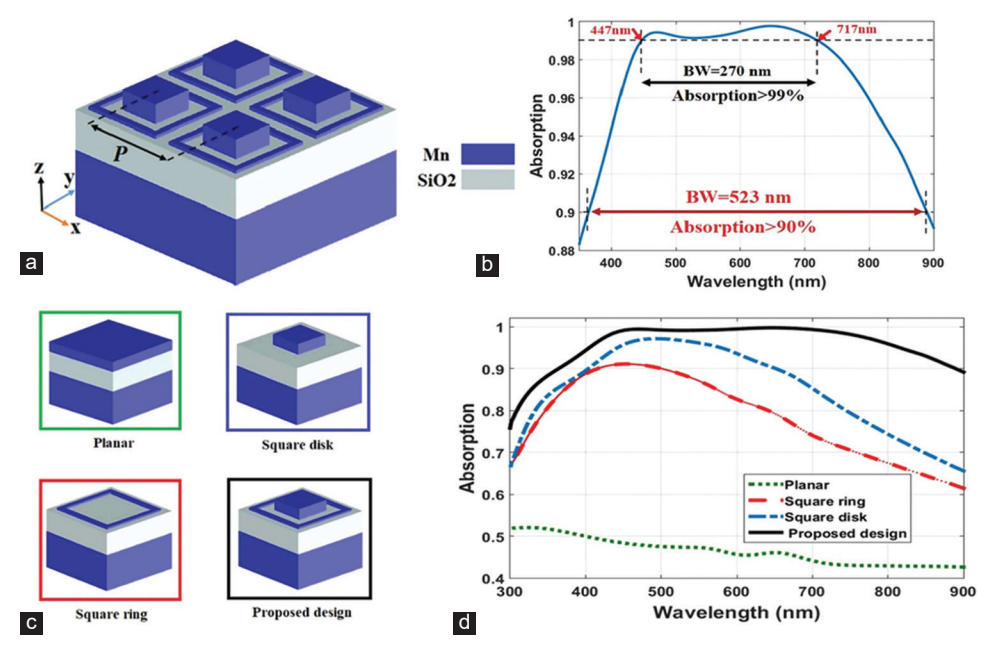


Fig. 12. (a) Illustrative diagram of a periodic arrangement of the proposed broadband metamaterial absorber, (b) Absorption performance of the proposed absorber design using optimized parameters, (c) A 3-D representation of three distinct absorber configurations utilizing the proposed design, and (d) Absorption spectra for all three configurations, incorporating the proposed design (Sayed, et al., 2023).

harvesting.

A new approach to developing broadband prefect absorbers depends on an array of nanospheres from visible to IR regions introduced by (Zhou, et al., 2023). This theoretical approach is based on the self-assembly nanostructure technique to compose a MIM configuration. The configuration of a metal layer (Pt), a layer of submicron polystyrene spheres, an insulator layer (Al₂O₂), and another metallic layer (Au) is as shown in Fig. 13a and b. The Nobel metals (Pt and Au) are traditionally used in plasmonic material at desired regions due to their large Q-value. The COMSOL Multiphysics software was employed to analyze and examine the absorber's parameters. To explore the effectiveness of an array structure consisting of self-assembled nanospheres two designs were proposed. The first design used 65 nm of Pt metal to be deposited on top of the polymer spheres, aiming at forming a MIM plasma structure, while the second one was without Pt, as shown in Fig. 13c. Noteworthy, the proposed design with the Pt metal on top achieved an average absorption of over 95%.

In the wavelength range from 400 nm to 1400 nm, the authors analyzed the electromagnetic field distribution within the designed structure at three different wavelengths (530, 890, and 1210 nm) to study the physical mechanism of the absorber. The electric field distribution shown in Fig. 13d-f, demonstrates the concentration of the strong electric field at the gap between nanosphere. When the wavelength is increased, the field is propagated toward the top surface of the metal spherical shell (Fig. 13f). The excited metallic spherical shells produce an electric dipole, leading to an electric dipole resonance at certain wavelengths. The LSPR effectively amplifies the absorption of light. Above the structure, the magnetic field (Fig. 13g-i) is highest, and it

shifts as the wavelength increases. LSPR creates surface plasmonic excitations (PSPs) below the structure, resulting in enhanced absorption. There is also reflection of light between the Pt and Au layers, creating a resonant cavity that enhances absorption in the near-IR range (Fig. 13i). Additionally, the design of the absorber demonstrates relative insensitivity to incoming angles, maintaining high absorption levels even at angles as high as 30 degrees.

The reviewed categories of BMMAs highlighted different design strategies explored in recent works to provide a clear overview of their performance. Table I shows a comparative summary of the representative works in terms of Bandwidth, polarization independence, incident angle, and integration capability. It is obvious from the comparative results that integration of BMMAs in OSCs depends mainly on their operating range and lumped elements of BMMAs. The bulk design is less suitable for compact integration due to operating mainly in microwave and terahertz regions. Consequently, the focus of research shifts to planar, vertical, and plasmonic nanostructures. Hence, BMMAs having low profiles are capable of operating in the optical to IR regions.

VIII. BMMAs in OSCs

The development of MMAs in 2008 unlocked opportunities for various applications, such as energy harvesting devices, photodetectors, and more. Those absorbers manipulate electromagnetic waves, specifically the light trapping and absorption. OSCs are well acknowledged for their flexibility, lightweight structure, and lower manufacturing costs. However, efficiency and stability remain a significant challenge. The integration of BMMAs into organic photovoltaic (OPV) can offer a promising solution to these

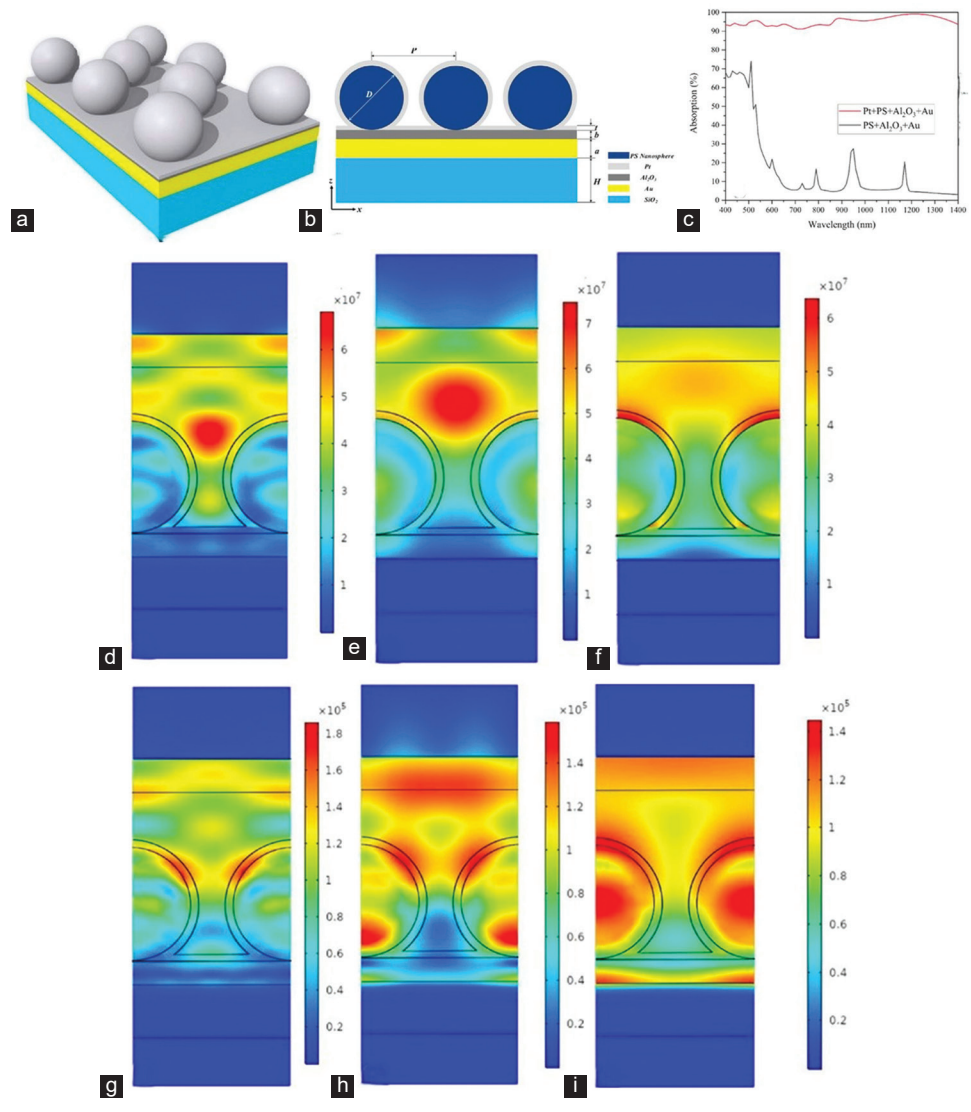


Fig. 13. Diagram of the proposed absorber structure: (a) 3D perspective, (b) Side view, (c) Absorption properties of the absorber, and (c) Absorption curves for various absorber configurations. Electric field distribution at various wavelengths: (d) 530 nm, (e) 890 nm, and (f) 1210 nm. Magnetic field distribution at different wavelengths: (g) 530 nm, (h) 890 nm, and (i) 1210 nm (Zhou, et al., 2023).

issues. Upon the inclusion of MMs, the absorption can be expanded beyond the visible spectrum to the IR region. Furthermore, the absorber's independence in polarization and incident angle can maintain the absorption rate. Next-generation OPVs with broadband MMs could significantly improve light collection, accelerate photon conversion to electrons, and enable tunable properties, thereby deriving further advancement in solar cell technologies.

Along this line, researchers (Liu, et al., 2013) investigated a broad-angle and polarization-independent perfect absorber with hybrid metal-dielectric-metal configurations. This work aimed to achieve improved absorption in the visible region that remains independent of the incoming angle and polarization. The structure consists of nanopattern arrays of Al as the top layer, a flat layer of Al in the ground layer, and the active layer of OPV (P3HT: PC60BM), which is positioned between metallic layers. To assess the absorber's performance, the study employed computational modeling using rigorous coupled-wave analysis (RCWA) and the FEM

to investigate the structural effects of absorption enhancement (AE). The total absorption $(A(\lambda))$ of thin OPV was expressed as the sum of the absorption of the metallic nanostructure (A metal (λ)) and the active layer OPV thin film (AOPV (λ)). The impact of nanopattern with different widths (W = 60, 70,80, and 90 nm) and those without patterns was examined. It was seen that those active layers with nanopatterns showed a maximum absorption, $A(\lambda)$, and the enhancement was mainly occurred at a width of 70 nm, which is suitable for the absorption spectrum of 40 nm thick active layer. Another task is to examine angular independence to determine the viability of achieving omnidirectional absorption, thereby employing P-polarization incidence. Adding Al nanopatterns to the P3HT: PC60BM layer allows the hybrid metal-OPV system to exhibit a 91% absorption peak at 500 nm. This is within the effective absorption band of the P3HT: PC60BM material (i.e., lower 650 nm). The OPV layer for p-polarized incidence showed that the layer has absorbed more than 70% of the incident energy up to 60° of the incident angle. The

TABLE I
COMPARISON OF RECENT BROADBAND METAMATERIAL ABSORBERS

MMBA category	Bandwidth (>90%)	Polarization independent	Angle stability (°)	Integration capability
Planar	400–1100 nm	Not reported	60	Heat production device (Takashima, et al., 2024)
Planar	525–2275 nm	Yes	θ≤70	Photovoltaic devices, Photonic detector (Liao, et al., 2024)
Planar	400–785 nm	Not reported	θ≤70	Optical devices (Sayed, et al., 2025)
Planar	11.09-108.2 GHz	Yes	45	Stealth technologies (Zhao, et al., 2025)
Vertical	0.2–4.5 μm	Low dependent	50	Solar/Thermal energy devices (Karimi Habil, Ghahremani and Zapata-Rodríguez, 2022)
Vertical	300-2500 nm	Low dependent	60	Solar/renewable energy devices (Wang, et al., 2023b)
Vertical	2.5–22 μm	Yes	70 (TM) 50 (TE)	Not specified (Abouelez, Eldiwany and Swillam, 2024)
Vertical	9.68-17.45 GHz	Yes	45	Power harvesting, stealth technologies (Bağmancı, et al., 2024)
Vertical	7–18 GHz	Low dependent	θ≤60	Not specified (Long, et al., 2016)
Plasmonic-nanostructure	400–800 nm	Yes	60	Solar PV system, heat emission (Armghan, Aliqab and Alsharari, 2025)
Plasmonic-nanostructure	400-750nm	Yes	60	Solar photovoltaic (Kumar, Singh and Pandey, 2022)
Plasmonic-nanostructure	400–2800 nm	Yes	60	Heat-based image, Solar/Thermal harvesting (Bilal, et al., 2022)
Plasmonic-nanostructure	400–2400 nm	Yes	45	Solar power conversion, Optical communication (Musa, et al., 2023)
Plasmonic-nanostructure	380–2300 nm	Yes	70	Detection devices, Heat emitter (Hanif, et al., 2024)
Lumped elements	1.33–3.57 GHz	Yes	40	Wireless network, Radar technology, Satellite system (Ardeshana, Thakkar and Domadia, 2025)
Lumped elements	8-16 GHz	Yes	45	Industrial uses (Baqir, et al., 2025)
Lumped elements	8.46-16.21 GHz	Yes	40	Radar Technology, Stealth system (Islam, Rahimian and Ho, 2025)
Lumped elements	2.7-12.7 GHz	Yes	θ≤40	Radar technology, EM shielding (Zhang, et al., 2023)

S-polarization of the magnetic field directions faced a shift when the angular incident was increased. Because of this, the retention resonance has different properties for the two polarization states, especially when the incident angle is higher. Furthermore, adding nanostructure to the active layer allows it to absorb 1.73–2.88 times extra light across a wide range of incident angles and polarization states.

On the other hand, (Liu, et al., 2014) studied theoretical designs to achieve high absorption in extremely thin OPV films. In this work, authors used a variety of planar structures to achieve a high absorption that remains independent on polarization and incoming light across visible regions. The first structure consists of a top nanopatterned (Al) square array on the OPV active layer (P3HT: PC60BM), with a bottom flat (Al) as the ground plate. The width of the nanopattern is crucial for absorption; an optimal width of 70 nm demonstrates the maximum absorption of the OPV layer at wavelengths of 500 nm and with incoming angles up to 60°. The second structure of double nanopatterns consists of 2D nanosquares (Al) at the top layer, nanoholes (Al) in the bottom layer, and active layer sandwiches between layers, as shown in Fig. 14a. The total absorption spectra $A(\lambda)$ for the whole device and $AOPV(\lambda)$ for the active OPV layers are plotted in Fig. 14b for various widths, with the period (P) and diameter (D) of the bottom aluminum nanohole array set at 240 nm and 120 nm, respectively. For top aluminum nanosquares sized 70 nm in width, the double nanostructure absorption $A(\lambda)$ device showed a slightly higher absorption in 400-500 nm with greatly improved one in 600-700 nm. This is where the absorption at 600 nm has increased from 60% to 95%. On the other hand, the 600-700 nm range enhances the absorption of the active layer AOPV(λ). The angular independent of total absorption (A total) for the optimized double nanostructure was modeled for both S and

P polarization. The results showed an average absorption band (450–600 nm) of more than 95% for incoming angles up to 50° and more than 85% for angles up to 70° (Fig. 14c). The charge distribution at the resonant wavelength of 580 nm has been calculated to explain the underlying principles of the device absorber, as illustrated in Fig. 14d. The upper aluminum nanosquares and the lower aluminum nanohole array induce anti-parallel currents. This process induces circulating currents among these metallic layers. This creates an artificial magnetic moment that significantly interacts with the incoming light's magnetic field, resulting in improved confinement of the electromagnetic field. Furthermore, to fully separate the absorption of the active layer from metal losses, the angular independent of the absorption of the active layer, $AOPV(\lambda)$, and metal absorption, $Ametal(\lambda)$, was analyzed. Fig. 14e shows that the active layer achieved an absorption peak exceeding 60% for angles up to 40° at a wavelength of 500 nm. However, as the incoming angle increases from 40° to 75°, metals absorb more than 40% (Fig. 14f). More than 60% of absorbed energy in the 615-700 nm range belongs to metal losses. This falls outside the effective absorption range of P3HT (Eg. = 1.9 eV or 650 nm). To illustrate the practicality of high absorption within a fully integrated device architecture, a layer of 100 nm-thick ITO was put on top of the structure, as depicted in Fig. 14a, which showed a similar angle-insensitive AE (the similar data is not displayed here).

The authors added an ITO layer to explore its practical integration. Although they did not provide detailed results to verify the outcomes. Instead, they suggested that a similar outcome is achievable, resulting in a gab in exhibiting the absorber's performance through practical applications.

In another interesting work (Zhang, et al., 2015), researchers explored the integration of the active layer of

ARO p-ISSN: 2410-9355, e-ISSN: 2307-549X

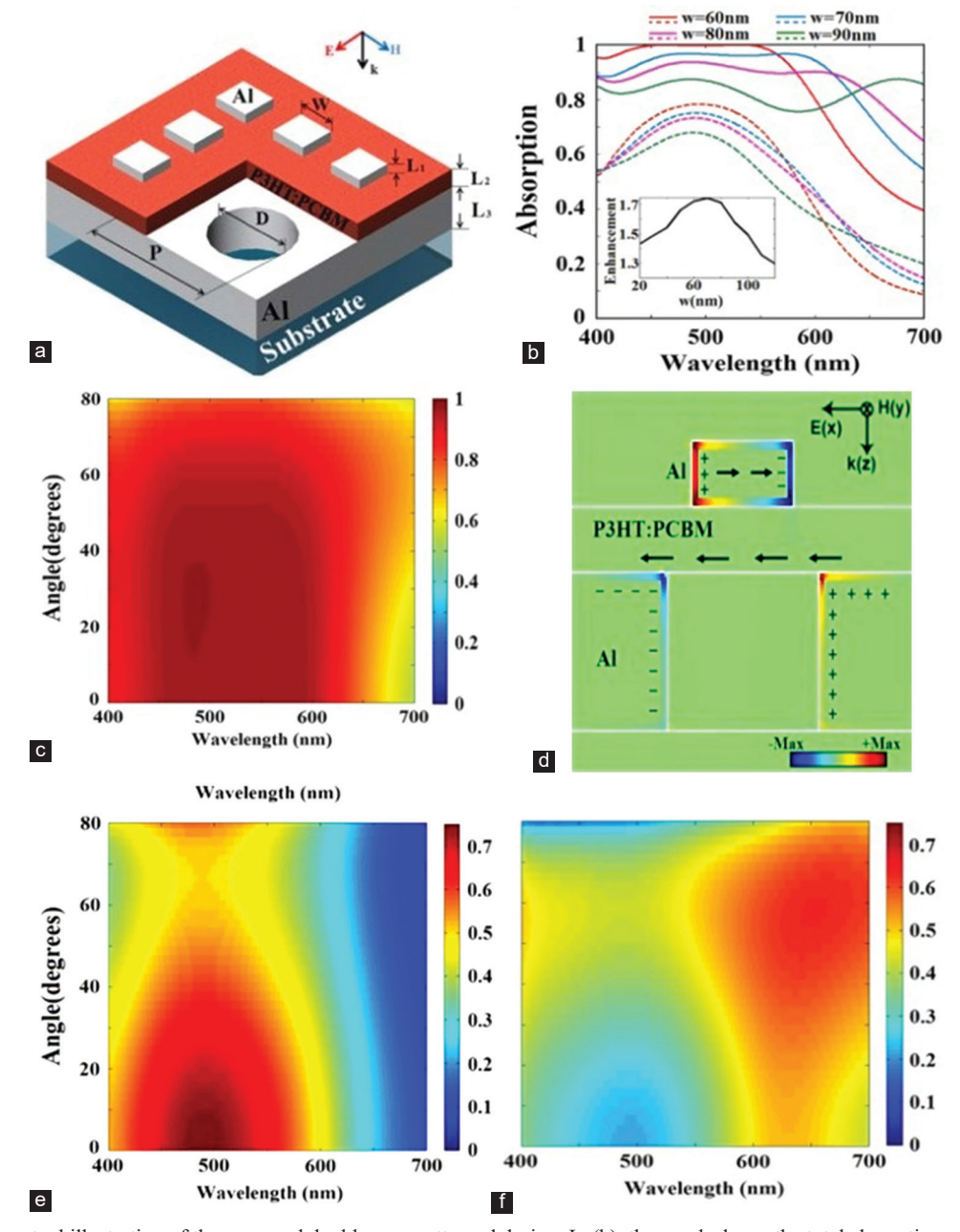


Fig. 14. (a) A conceptual illustration of the proposed double nanopatterned design. In (b), the graph shows the total absorption spectra of the organic photovoltaic (OPV) device (A(λ); solid lines) and OPV active layers (AOPV(λ); dashed lines) at various widths (W = 60, 70, 80, and 90 nm) under normal light exposure. In (c), the angular dependence of the total absorption (Atotal) for the entire OPV device, which includes optimized aluminum nanosquares on the top (W = 70 nm) and aluminum nanohole arrays in the bottom (P = 240 nm). (d) shows the charge distribution calculated at the 580 nm resonance absorption wavelength. (e and f) represent the angular dependence of the selective absorption. (e) depicts the P3HT active layer, while (f) showcases metals with optimized bottom aluminum nanohole arrays and top aluminum nanosquares (Liu, et al., 2013).

OSCs and magnetic MMs to enhance the optical absorption in thin OPV. They introduced a structure where two metal electrodes (Ag) are configured in a periodic grating pattern to sandwich the thin OSC's active layer (P3HT: PCBM), as depicted in Fig. 15a. This design supports both electric resonance and magnetic resonance, which enhances electromagnetic absorption across a wide spectrum range. A numerical simulation using COMSOL Multiphysics confirms broadband spectrum with two separate peak absorption values at 425 and 590 nm, as shown in Fig. 15b. In

devices without MMs, there is only one peak around 480 nm. This shows how important MMs are for achieving dual-peak broadband absorption and improving light capture across a wider spectrum. The absorption peak at 590 nm showed that the enhancement factor is notably higher, approximately 6.2, and about 20% greater at 425 nm. This significant difference is due to a strong interaction between the incoming light and device at higher wavelengths (Fig. 15b). The magnetic field distributions and electric displacements are shown in Fig. 15c and d. Fig. 15c shows that surface plasmons

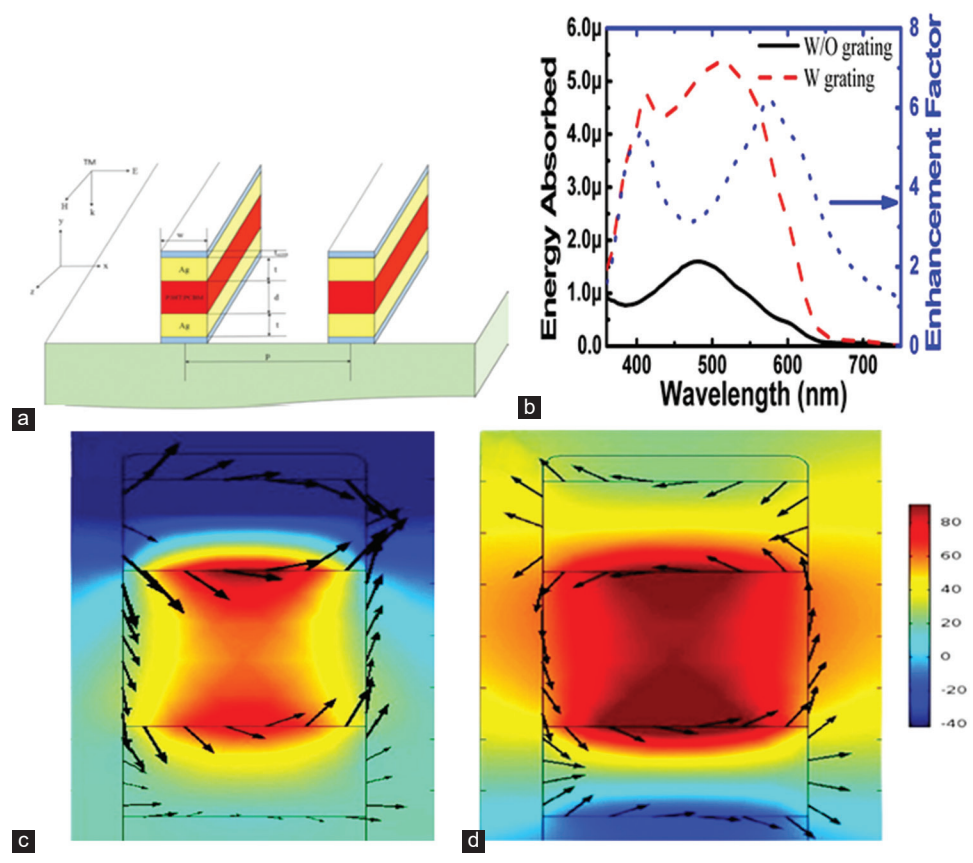


Fig. 15. (a) A three-dimensional representation of the structure, (b) The electromagnetic energy loss for the organic active material, both with and without the grating, along with the wavelength-dependent factor for absorption enhancement. The distribution of the magnetic field and the electric displacement within the metamaterial-based solar cell structure at (c) 425 nm and (d) 575 nm (Zhang, et al., 2015).

predominantly confine energy at the interface between the organic layer and the top metal electrode. Conversely, the magnetic resonance (Fig. 14d) resulted in more uniform energy distribution across the organic layer. Furthermore, for the resonance wavelength 575 nm, the absorbance enhanced factor was >7 at an incident angle of 10°. However, this factor consistently decreases as the incident light angle increases. The AE factor remains above 2 for the range 450–650 nm, up to angle 50°. The same behavior can be seen for 425 nm with an absorbance factor above 2 for incident angle 40°. Above this angle, the absorbance factor is rapidly declining. reveals that AE s show that they are particularly robust at normal incidence angles above 70°.

Other researchers (Katsumata, et al., 2020) investigated the role of MMPAs in improving the performance of OSCs, particularly in the PCPDTBT: PC71BM OSC, by broadening their light absorption capabilities across a wide frequency range. The device is built on a SiO₂ substrate, which is followed by layers of ITO, silver nanostrips, thin ZnO films, PCPDTBT, PC71BM, and MoO₃. Finally, an aluminum (Al) layer is added on top. Various MPA solar cells embedded with Ag nanospheres have pitches of 350, 400, and 500 nm. The absorption properties of the MPA solar cells were analyzed using UV-vis-NIR spectroscopy. The measurement taken from substrate side, showed higher absorption values for TE polarization as compared to TM polarization. This

implies the existence of various surface plasmon types, including Al surface plasmons and localized Ag NS surface plasmons. The study examines the relationship between AE and IPCE (incident-photon to current efficiency) in MPA devices across 400-1000 nm, from wavelength 830 and 990 nm, the AE and IPCE ratios for MPA solar cells featuring 500 nm-pitch silver nanospheres (Ag NSs) exceeded unity. This suggests that an increased AE has led to an enhanced IPCE. However, in the 580-830 nm range, the AE is still up trending, while the IPCE is lower. This indicates an inverse relation. The 450 and 350 nm-pitch silver nanospheres (Ag NSs) solar cells exhibited a similar trend. This indicates that the AE induced by Ag NSs affects IPCE differently across different wavelengths. The numerical simulation was used to calculate the AE and magnetic field distribution through the cell structure. The field distribution for 500 nm-patched Ag nanostructure solar cells at 756 and 932 was in investigated. It was observed that at 756 nm, the magnetic field was localized on the surface of Ag-NSs, close to the ITO layer (Fig. 16a and b). This suggests the presence of LSPR. The active layer traps the field at 932 nm in a magnetic resonance mode, enhancing light absorption, as shown in Fig. 16c and d. For 400 nm-pitch NSs, the magnetic field is placed at the rear side of the NSs structure at 696 nm and at weak resonance at 812 nm. A 350 nm-pitch Ag NS solar cell (Fig. 16e and f) fits the same description. This suggests

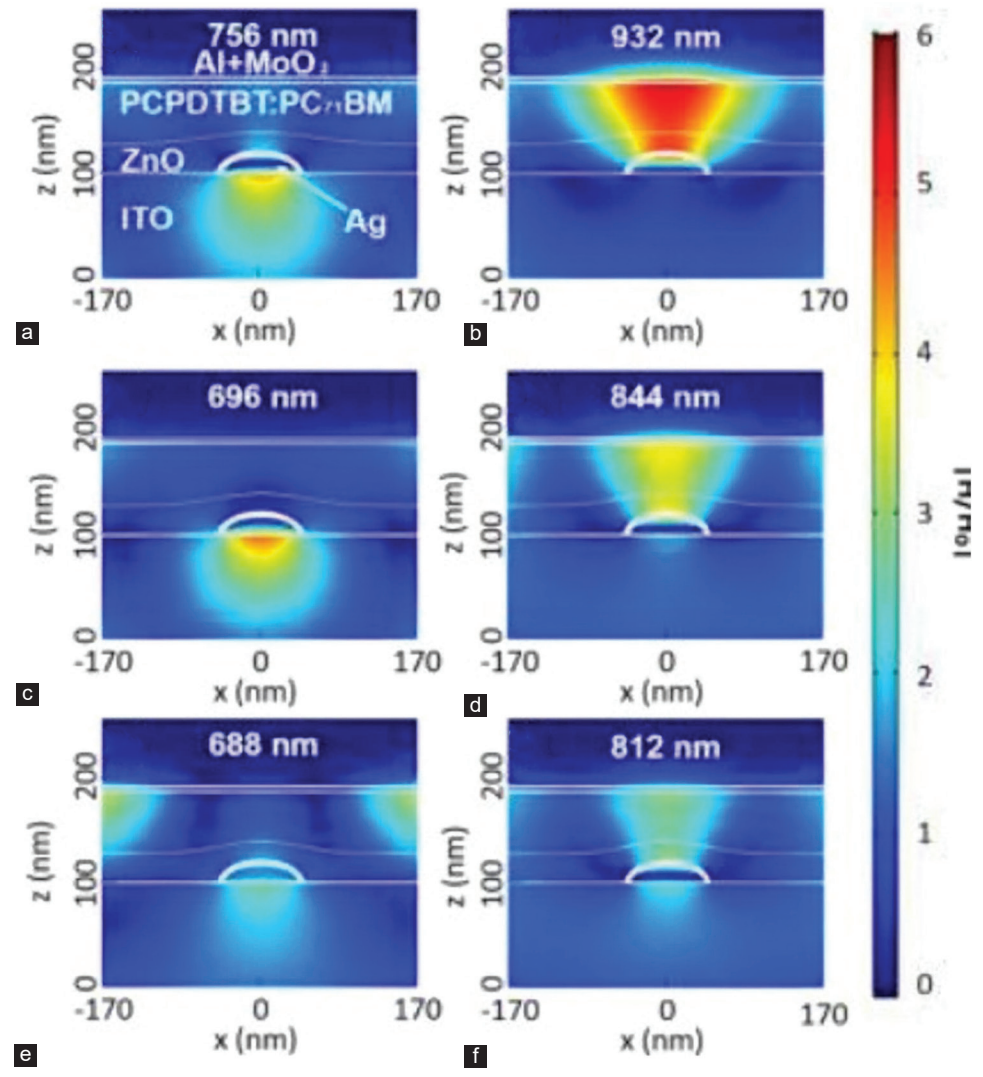


Fig. 16. Magnetic field distributions in metamaterial prefect absorber solar cells containing silver nanospheres (Ag NSs) with pitches of (a and b) 500 nm, (c and d) 400 nm, and (e and f) 350 nm. The magnetic fields were computed at wavelengths of (a) 756 nm, (b) 932 nm, (c) 696 nm, (d) 844 nm, (e) 688 nm, and (f) 812 nm, respectively (Katsumata, et al., 2020).

that the magnetic resonance improves light confinement in the active layer for long wavelengths. With varying Ag NS pitches, the device's performance varied slightly; the sample with the 350 nm pitch had the best PCE, at 2.03%.

In a different study (Isegawa, et al., 2019), researchers embedded silver nanostrips (Ag NSs) into OSCs active layers made of P3HT: PC61BM, aiming at enhancing the absorption performance. The solar cell structure was composed of several layers, starting with an ITO-coated glass substrate, followed by a layer of Ag NSs, ZnO, P3HT: PC61BM as the active layer, MoO₃, and Al as the electrode, as illustrated in Fig. 17a. The Scanning Electron Microscopy revealed the Ag NSs with a width and pitch of 82 and 500 nm, respectively, as can be seen in Fig. 17b. A spectroscope was used to measure the reflection spectra for both TE and TM polarization, and hence to analyze the impact of Ag nanostructure on solar cell optical properties. At wavelengths between 400 and 900 nm, the reflectance spectrum for TE polarization in solar cells with nanostrips was lower than that for TM

polarization. This range corresponds to the absorption band for P3HT: PC61BM. The reflectance spectrum of solar cells without Ag NSs showed a higher reflectance as compared with solar cells with Ag nanostrips (higher absorption). This indicates a significant enhancement of light absorption due to the presence of Ag nanostrips in such cells. The AE parameter (represents the ratio of cell absorption of TE to TM). The AE parameter variation with wavelength corresponds to the measured absorption spectrum of both P3HT and P3HT: PC61BM, as shown in Fig. 17c. The AE 1.12 at 600 nm correlates with P3HT extreme absorption, and it reaches 1.2 in the wavelength range between 600 nm and 650 nm. This suggests that Ag-nanostrips can enhance the absorption by 20% when compared to P3HT alone. The theoretical simulation in this work employs RCWA to elucidate the absorption feature. Both calculated and measured AE depend on the Ag NSs pitch. Over the wavelength range of 500-650 nm, for averaged the AE factor. While the AE showed a significant difference when the nanostrips with

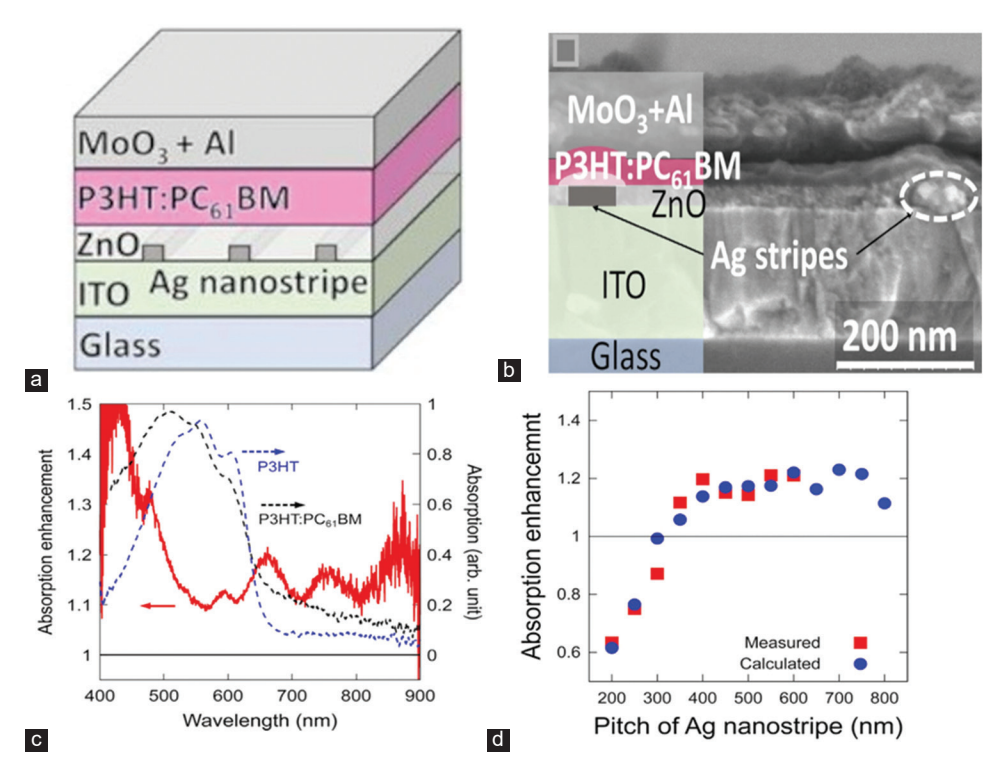


Fig. 17. Representation of the P3HT: PC61BM solar cell including Ag nanostrips, (b) Scanning Electron Microscopy image of the cell in cross-section. The silver nanostripe was delineated by a white dotted line, (c) The absorption enhancement observed in the P3HT: PC61BM solar cell integrated with Ag nanostripes is represented on the left axis, while the dashed lines depict the measured absorption spectrum of a P3HT: The film of PC61BM is represented by the black dashed curve, while the P3HT film is indicated by the blue dashed curve, corresponding to the right axis. (d) Measured and simulated the average absorption enhancements of P3HT: PC61BM solar cells incorporating Ag nanostripes, varying with respect to their pitches (Isegawa, et al., 2019).

solar cells were shorter than 350 nm, nanostrip with longer than 350 nm had not significantly influence on AE, as shown in Fig. 17d. In addition, the calculated and measured AE a cross Ag- nanostrip width (60–120 nm) showed similar behavior. This suggests that the cell device's absorbance is dependent on the pitch width. Furthermore, the measured P3HT: PC61BM thickness layer, which ranges from 29 to 80 nm within the AE parameter between 1.1 and 1.2, suggests that the measured active layer thickness does not have a significant impact on the results. On the other hand, as the pitch gets thinner, the calculated AE increases linearly.

Furthermore, while the integration of MPA in OSCs theoretically and experimentally demonstrated a 20% increase in absorption. The authors conclude that further research is necessary to connect the optical enhancement and practical impact of MPA on solar cells.

Other researchers explored the use of hyperbolic MMs (HMM) in OSCs to improve light absorption exciton generation (Chao, et al., 2023). The HMM structure consists of multiple MoO₃/Au stack pairs which exhibits hyperbolic dispersion to improve light absorption within the active layer. The first stacked pair of MoO₃/Au from HMM acts as a hole transport layer. The solar cell structure is composed of several layers, starting with an ITO as substrate, followed by a layer ZnO, P3HT: PC61BM as the active layer, and four pairs of (MoO₃/Au), as shown in Fig. 18a. In contrast,

the reference device uses a single pair of MoO₃/Ag in solar cell configuration. The performance of HMM-OGSs under standard lighting conditions was compared with the reference device. Fig. 18b illustrates the current density-voltage (J-V) of the device's performance. The reference OSCs exhibited these characteristics: an open-circuit voltage (V_{OC}) of 0.53 V, a shortcircuit current density (J_{SC}) of 9.88 mA/cm², and a fill factor (FF) of 58.57%. These parameters collectively contributed to a PCE of 3.06%. for HMM-OSCs, the values of V_{OC} , J_{SC} , and FF were 0.53 V, 10.53 mA/cm², and 62.16%, respectively, within PC of 3.39%. There was moderate enhancement for both J_{sc} and FF by 6.6% and 6.1%, respectively. This resulted in an increase of 11% in HMM-OGS's PCE. The study confirms that the enhancement is due to broader absorption at 450-650 nm with a maximum improvement of 7% at $\lambda = 600$ nm, as demonstrated by external quantum efficiency measurements for both devices (Fig. 18c). Photoluminescence (PL) measurements have been used to explain the impact of HMM on excitons generation for both structures. Fig. 18d shows the PL spectra for both devices. Using a 530 nm light wavelength source at room temperature to illuminate both samples, the HMM integrated PL intensity improved by 25% compared to the pristine device. This indicates that the device with HMM structure absorbs more photons and generates more excitons compared to the reference device. The researchers employed Lumerical, a commercial electromagnetic simulation software

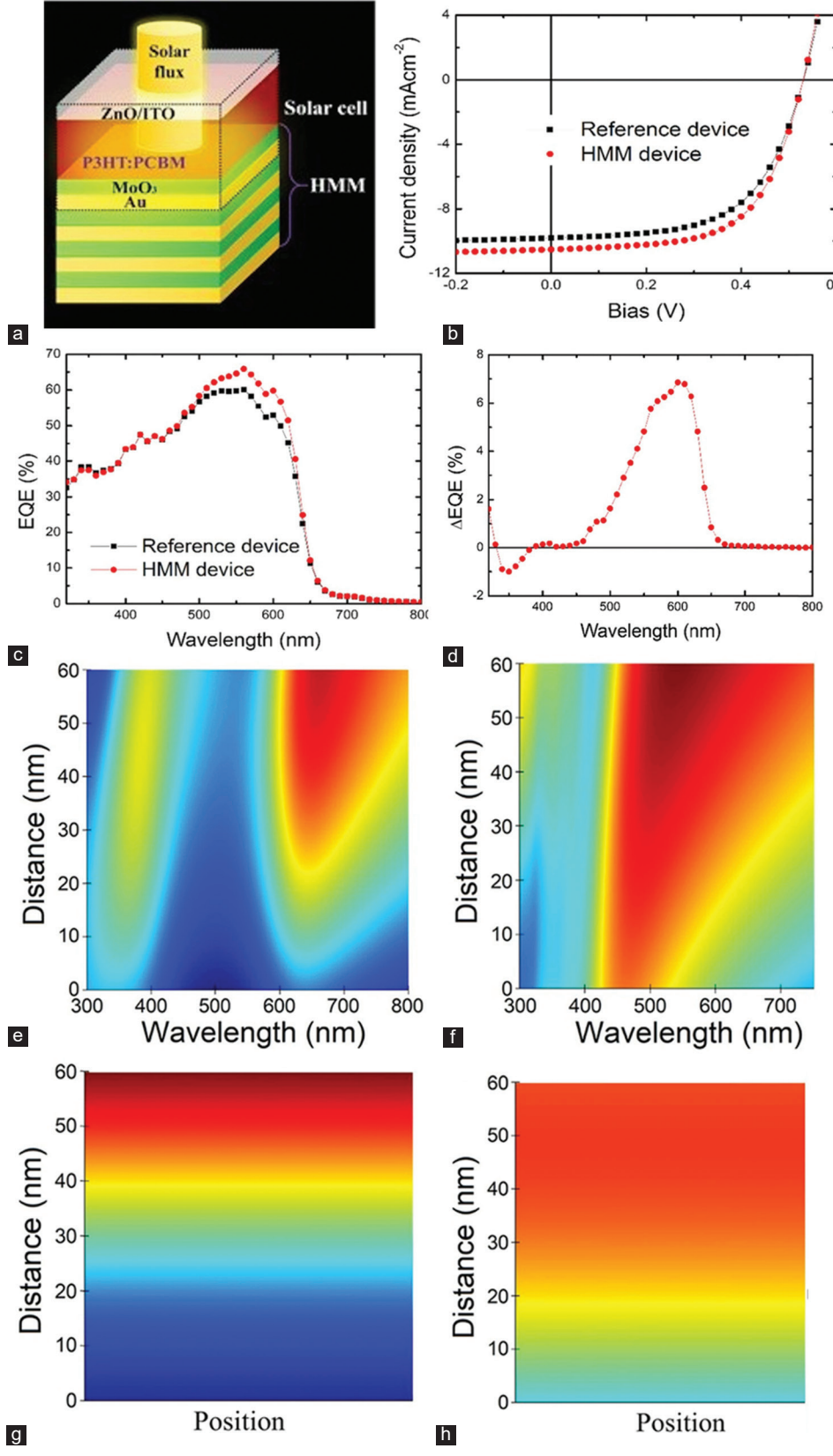


Fig. 18. (a) Diagram showing the structure of the proposed device. (b) The current density–voltage (J-V) curve characteristics of the optimal reference cell and hyperbolic metamaterial-organic solar cell (HMM-OSC) illuminated by AM 1.5G at 100 mW cm². (c) The reference and HMM-OSC devices' external quantum efficiency spectrum (d) photoluminescence spectra of the P3HT: PCBM layer deposited on MoO₃/Ag and the HMM structures fabricated on Si wafers with an excitation wavelength of 532 nm. The electric-field distributions, varying with wavelength, as a function of distance from the top surfaces of (e) MoO₃/Ag and (f) HMM structures with P3HT: PCBM. The electron-hole pair generation rate distributions as a function of distance from the top surfaces of (g) MoO₃/Ag and (h) HMM in P3HT: PCBM structure (Chao, et al., 2023).

that is based on a finite-difference time-domain approach to support measurement results. The electric field distribution is shown for both structures with and without HMM (reference sample) in the wavelength range of 300-800 nm, as shown in Fig. 18d-e. A plane wave source was applied from the top of each structure. The electric field around the HMM surface was stronger than in the reference sample. This suggests that BPP excitation inside the layered HMM structure makes the electromagnetic field near the HMM stronger. The local increase in electric field strength can enhance the ability of the photoactive layer to absorb light, leading to a higher production of excitons. For this reason, the exciton generation rate in the organic layer was estimated by calculating the absorption intensity. It was found that the reference sample (Fig. 18g) had an electron-hole pair generation rate of 1.24 × 10²⁸ m⁻³ s⁻¹, which means it had a current density (J₂₂) of 118.93 mA.cm⁻². On the other hand, the HMM structure (Fig. 18h) had a higher generation rate of 1.57×10^{28} m⁻³ s⁻¹ for a J₂ of 150.59 mA.cm⁻². This indicated that the generation rate went up by an average of 27% because the electric field distribution was better.

In summary, this study demonstrated the utilization of HMM to improve the performance of OSCs. However, the article does not address polarization insensitivity and angular insensitivity. These are critical considerations in real-world situations. Including such considerations could provide a comprehensive understanding of the device's performance efficiency.

IX. EXTENDED DISCUSSIONS

The review of literature demonstrated how MMA structures have been simulated and experimentally proved to be viable for the light trapping and enhancing absorption in organic active layers. This in turn leads to improve the overall efficiency of OSC devices. It is worth to mention that the majority of the studies relied on simulation-based approaches. However, a limited number of research works were based on experiential fabrication and numerical modelling. Concludingly, the combination of theoretical investigations and experimental validations offers a valuable insight for future real-world applications of MMAs in OSCs.

Three notable simulation-driven researches have explored ways to enhance light absorption in OSCs through the integration of MMAs. The researchers have shared a common MIM configuration. The structure consists of Al as a ground plane, a P3HT: PC60BM dielectric layer, and nanopattern arrays of Al as the top layer. The authors in (Liu, et al., 2013) demonstrated a broad-angle and polarization-independent operation in the visible region (400–700 nm), showing a strong absorption in the active layer. The previous work was later improved by (Liu, et al., 2014) modifying the design through introducing nanoholes in the ground-Al plane to further enhance the absorption, as can be seen in Fig. 14a. Simulations confirmed that the designs incorporating nanoholes have enhanced absorption compared to the original design (Fig. 14b). On the other

hand, Zhang, et al. adopted a different approach, which was realized by placing two patterned Ag electrodes in a periodic grating configuration that sandwiched P3HT: PCBM between them (Zhang, et al., 2015). In this way, both electronic and magnetic resonance were guaranteed to enhance the broadband absorption, as can be seen in Fig. 15b. Noticeably, the operating wavelength range remains in the visible region. The design's approach and field distribution characteristics differ from previous works. This difference highlights the variety of strategies available to improve light absorption in OSC structure through simulation-driven designs.

Recent studies have highlighted the role of plasmonic resonance in boosting OSC performance. Along this line, researchers utilized Ag nanospheres in a multilayer MPA design to excite both Ag plasmon modes and Al surface plasmons using varied pitches, ranging from 350 to 500 nm (Katsumata, et al., 2020). This approach was used to extend the enhancement of light absorption to the NIR region (400 to 1000 nm), with strong confinement occurring at 932 nm, as shown in Fig. 16b. Interestingly, a PCE of 2.03% was achieved for the 350 nm pitch. In another relevant study (Isegawa, et al., 2019), researchers replaced the Ag nanosphere with the Ag nanostrip under the P3HT: PC61BM active layer. This configuration could improve light absorption in the range of 400-900 nm for the TE mode. Fig. 17d shows that the strip pitch is a key parameter, by which a thinner pitch provided a higher AE factor compared to work reported elsewhere (Katsumata, et al., 2020). This approach was able to yield 20% higher absorption in the targeted spectral range. Moreover, (Chao, et al., 2023) employed a HMM stack pair of MoO₃/Au below the P3HT: PC61BM active layer, thereby improving the PCE by 11% through broadband field confinement in the range of 400–650 nm, as shown in Fig. 18c. Comparably, the first two works were focused on plasmonic resonance tuning, while the third one relied on anisotropic dispersion in the HMM structure.

X. CHALLENGES AND FUTURE DIRECTIONS

Noticeably, most of the published works in the literature were able to achieve a narrow to moderate absorption band rather than a broadband absorption that falls within the optical and NIR spectra. Nevertheless, one of the main key limitations is the MM design and the choice of the compatible active layer type. Gold and silver give strong plasmonic responses, but their high cost and poor stability limit their wide practical use. Alternatives such as TiN or Ni are more affordable and mechanically robust, yet they still face the issue of significant optical losses in the visible range. Achieving polarizationindependent and wide-angle absorption, along with smooth incorporation into active OSC layers, remains a challenge due to exciton diffusion limits. Moreover, most designs are currently only theoretical and untested experimentally. Further research should focus on low-loss refractory materials, hybrid plasmonic-dielectric scheme, and shift from a purely theoretical model to an experimental validation. At the same time, despite those limitations, the continued development of MMAs offers a promising pathway toward the next generation of OSCs. If these challenges can be solved, BMMAs could provide tunable broadband absorption with flexible design options, making them a strong candidate for boosting OSC performance.

XI. CONCLUSION

This review highlighted the exciting potential of BMMAs (MMBAs) to address some of the challenges that currently exist in OSC technology. These absorbers have the ability to significantly enhance light absorption and boost energy conversion efficiency, particularly by capturing a wider spectrum of light. However, despite these promising advancements, the current research in this area is still in its early stages. Most of what we know comes from theoretical models and simulations, while real-world applications remain underexplored. Only a small number of studies have ventured into the practical integration of MMBA designs into OSCs, and even fewer have delved into the concept of perfect absorbers. This leaves a noticeable gap between the potential of these technologies and their actual implementation. Looking ahead, there is a clear need for more hands-on, experimental work to validate the findings from simulations and theoretical studies. Research should focus on understanding how to scale up these designs for mass production while maintaining their efficiency. This includes developing cost-effective and sustainable manufacturing methods to bring these innovative solutions to market. In addition, further exploration of how different material properties and design configurations influence light absorption will be key to refining and optimizing these technologies. Bridging these gaps is not just about improving OSCs, it is about paving the way for a cleaner, more sustainable future. As the demand for renewable energy continues to grow, innovations like MMBA technology could play a critical role in making solar power more efficient and accessible. By turning theoretical advancements into practical solutions, we can take a significant step forward in the global effort to harness renewable energy and reduce our reliance on fossil fuels.

REFERENCES

Aalizadeh, M., Khavasi, A., Butun, B., and Ozbay, E., 2018. Large-area, cost-effective, ultra-broadband perfect absorber utilizing manganese in metal-insulator-metal structure. *Scientific Reports*, 8(1), p.9162.

Abouelez, A.E., Eldiwany, E.A., and Swillam, M.A., 2024. Silicon-based ultra-broadband mid-IR and LWIR near-perfect metamaterial absorber. *Optical and Quantum Electronics*, 56(7), p.1103.

Ahmad, A., Asad, A., Pacpaco, P., Thampongphan, C., and Hasan, M.H., 2024. application of metamaterial in renewable energy: A review. *International Journal of Engineering Materials and Manufacture*, 9(2), pp.60-80.

Al-Badri, K.S.L., 2020. Electromagnetic broad band absorber based on metamaterial and lumped resistance. *Journal of King Saud University-Science*, 32(1), pp.501-506.

Ali, A., Mitra, A., and Aïssa, B., 2022. Metamaterials and metasurfaces: A review from the perspectives of materials, mechanisms and advanced metadevices.

Nanomaterials (Basel), 12(6), p.1027.

Aliqab, K., Armghan, A., and Alsharari, M., 2024. Polarization insensitive and wideband terahertz absorber using high-impedance resistive material of RuO₂. *Scientific Reports*, 14(1), p.19149.

Ardeshana, M.A., Thakkar, F.N., and Domadia, S.G., 2025. Composite structure design for broadband metamaterial absorption: Integrated nonlinearity and enhanced performance using lumped resistors. *Journal of Applied Physics*, 137(9), p.093104.

Armghan, A., Aliqab, K., and Alsharari, M., 2025. A novel fan-shaped ultrabroadband solar absorber using nickel-based plasmonic metasurfaces. *Scientific Reports*, 15(1), p.21839.

Bağmancı, M., Wang, L., Sabah, C., Karaaslan, M., Paul, L.C., Rani, T., and Unal, E., 2024. Broadband multi-layered stepped cone shaped metamaterial absorber for energy harvesting and stealth applications. *Engineering Reports*, 6(11), p.e12903.

Baqir, M.A., Qadeer, A., Altintas, O., Draz, M.U., Karaaslan, M., and Sampe, J., 2025. Design of polarization-insensitive wideband metamaterial radar absorber with enhanced bandwidth. *Progress in Electromagnetics Research C*, 155, pp.67-74.

Bilal, R.M.H., Saeed, M.A., Naveed, M.A., Zubair, M., Mehmood, M.Q., and Massoud, Y., 2022. Nickel-based high-bandwidth nanostructured metamaterial absorber for visible and infrared spectrum. *Nanomaterials (Basel)*, 12(19), p.3356.

Cai, B., Wu, L., Zhu, X., Cheng, Z., and Cheng, Y., 2024. Ultra-broadband and wide-angle plasmonic light absorber based on all-dielectric gallium arsenide (GaAs) metasurface in visible and near-infrared region. *Results in Physics*, 58, p.107509.

Carrillo-Sendejas, J.C., and Maldonado, J.L., 2025. Progress in organic solar cells: Materials, challenges, and novel strategies for niche applications. *APL Energy*, 3(2), p.021501.

Cen, C., Liu, X., Lin, Y., Yi, Z., and Zeng, Q., 2025. Metamaterial absorber with ultra-broadband, ultra-high absorption, polarization independence and high-temperature resistance for solar thermal energy harvesting applications. *Optics Communications*, 575, p.131292.

Chao, Y.C., Lin, H.I., Lin, J.Y., Tsao, Y.C., Liao, Y.M., Hsu, F.C., and Chen, Y.F., 2023. Unconventional organic solar cell structure based on hyperbolic metamaterial. *Journal of Materials Chemistry C*, 11(6), pp.2273-2281.

Chen, H.T., 2012. Interference theory of metamaterial perfect absorbers. *Optics Express*, 20(7), pp.7165-7172.

Chen, H.T., Padilla, W.J., Cich, M.J., Azad, A.K., Averitt, R.D., and Taylor, A.J., 2009. A metamaterial solid-state terahertz phase modulator. *Nature Photonics*, 3(3), pp.148-151.

Chen, Q., Huang, J.L., Wang, C.H., Ke, P.X., Yang, C.F., and Tseng, H.W., 2024. Investigation of a pyramid-like optical absorber with high absorptivity in the range of ultraviolet a to middle infrared. *Photonics*, 11(4), p.352.

Cheng, D.K., 1989. Field and Wave Electromagnetics. Pearson, Boston, MA, U.S.A., p.720.

Choukri, S., Takhedmit, H., El Mrabet, O., Aznabet, M., and Cirio, L., 2022. Wide Angle, Polarization Independent Metamaterial Absorber Unit-Cell for RCS Reduction and Energy Harvesting Applications. In: *The 12th International Conference on Metamaterials, Photonic Crystals and Plasmonics*. IEEE, Torremolinos, Spain, pp.1-8. Available from: https://hal.science/hal-03714453v1 [Last accessed on 2025 Aug 01].

Chowdhury, M.Z.B., Islam, M.T., Hoque, A., Alshammari, A.S., Alzamil, A., Alsaif, H., Alshammari, B.M., Hossain, I., and Samsuzzaman, M., 2022. Design and parametric analysis of a wide-angle and polarization insensitive ultrabroadband metamaterial absorber for visible optical wavelength applications. *Nanomaterials (Basel)*, 12(23), p.4253.

Duan, G., Schalch, J., Zhao, X., Li, A., Chen, C., Averitt, R.D., and Zhang, X.,

- 2019. A survey of theoretical models for terahertz electromagnetic metamaterial absorbers. Sensors and Actuators A: Physical, 287, pp.21-28.
- Duan, G., Schalch, J., Zhao, X., Zhang, J., Averitt, R., and Zhang, X., 2018. Identifying the perfect absorption of metamaterial absorbers. *Physical Review B*, 97(3), p.035128.
- Fu, X., and Cui, T.J., 2019. Recent progress on metamaterials: From effective medium model to real-time information processing system. *Progress in Quantum Electronics*, 67, p.100223.
- Gandhi, C., Babu, P.R., and Senthilnathan, K., 2021. Ultra-thin polarization independent broadband terahertz metamaterial absorber. *Frontiers of Optoelectronics*, 14(3), pp.288-297.
- Ghosh, S., and Srivastava, K.V., 2014. An equivalent circuit model of FSS-based metamaterial absorber using coupled line theory. *IEEE Antennas and Wireless Propagation Letters*, 14, pp.511-514.
- Góra, P., and Łopato, P., 2023. Metamaterials' application in sustainable technologies and an introduction to their influence on energy harvesting devices. *Applied Sciences*, 13(13), p.7742.
- Hanif, A., Alam, T., Islam, M.T., Hakim, M.L., Yahya, I., Albadran, S., Islam, M.S., and S. Soliman, M., 2024. Ni-PI-Ni based nanoarchitectonics near-perfect metamaterial absorber with incident angle stability for visible and near-infrared applications. *International Journal of Optomechatronics*, 18(1), p.2299026.
- Hoa, N.T.Q., Lam, P.H., Tung, P.D., Tuan, T.S., and Nguyen, H., 2019. Numerical study of a wide-angle and polarization-insensitive ultrabroadband metamaterial absorber in visible and near-infrared region. *IEEE Photonics Journal*, 11(1), pp.1-8.
- Huang, X., Zhang, X., Hu, Z., Aqeeli, M., and Alburaikan, A., 2015. Design of broadband and tunable terahertz absorbers based on graphene metasurface: Equivalent circuit model approach. *IET Microwaves, Antennas and Propagation*, 9(4), pp.307-312.
- Isegawa, T., Okamoto, T., Kondo, M., Katsumata, S., and Kubo, W., 2019. P3HT: PC61BM solar cell embedding silver nanostripes for light absorption enhancement. *Optics Communications*, 441, pp.21-25.
- Islam, K.M.R., Rahimian, A., and Ho, T.D., 2025. A low-profile wideband and polarization-insensitive metasurface absorber for X and Ku bands. *Journal of Electromagnetic Waves and Applications*, 39, pp.1534-1547.
- Jackson, J.D., 1999. Classical Electrodynamics. Wiley-VCH, United States of America.
- Jain, A., Kothari, R., Tyagi, V., Rajamony, R.K., Ahmad, M.S., Singh, H.M., Raina, S., and Pandey, A., 2024. Advances in organic solar cells: Materials, progress, challenges and amelioration for sustainable future. *Sustainable Energy Technologies and Assessments*, 63, p.103632.
- Jang, T., Youn, H., Shin, Y.J., and Guo, L.J., 2014. Transparent and flexible polarization-independent microwave broadband absorber. *Acs Photonics*, 1(3), pp.279-284.
- Jiao, S., Li, Y., Yang, H., and Xu, S., 2021. Numerical study of ultra-broadband wide-angle absorber. Results in Physics, 24, p.104146.
- Karimi Habil, M., Ghahremani, M., and Zapata-Rodríguez, C.J., 2022. Multioctave metasurface-based refractory superabsorber enhanced by a tapered unitcell structure. *Scientific Reports*, 12(1), p.17066.
- Katsumata, S., Isegawa, T., Okamoto, T., and Kubo, W., 2020. Effect of metamaterial perfect absorber on device performance of PCPDTBT: PC₇₁BM solar cell. *Physica Status Solidi (A) Applications and Materials Science*, 217(1), p.1900910.
- Kim, Y.J., Yoo, Y.J., Kim, K.W., Rhee, J.Y., Kim, Y.H., and Lee, Y., 2015. Dual broadband metamaterial absorber. *Optics Express*, 23(4), pp.3861-3868.
- Kishore, T.S., Kumar, P.U., and Ippili, V., 2025. Review of global sustainable solar energy policies: Significance and impact. *Innovation and Green*

- Development, 4(2), p.100224.
- Koschny, T., Kafesaki, M., Economou, E., and Soukoulis, C., 2004. Effective medium theory of left-handed materials. *Physical Review Letters*, 93(10), p.107402.
- Kotsuka, Y., 2019. Electromagnetic Wave Absorbers: Detailed Theories and Applications. John Wiley & Sons, Hoboken, New Jersey, USA, p.336.
- Kumar, R., Singh, B.K., and Pandey, P.C., 2022. Broadband metamaterial absorber in the visible region using a petal-shaped resonator for solar cell applications. *Physica E: Low-Dimensional Systems and Nanostructures*, 142, p.115327.
- Landy, N.I., Bingham, C.M., Tyler, T., Jokerst, N., Smith, D.R., and Padilla, W.J., 2009. Design, theory, and measurement of a polarization-insensitive absorber for terahertz imaging. *Physical Review B—Condensed Matter and Materials Physics*, 79(12), p.125104.
- Landy, N.I., Sajuyigbe, S., Mock, J.J., Smith, D.R., and Padilla, W.J., 2008. Perfect metamaterial absorber. *Physical Review Letters*, 100(20), p.207402.
- Lazaroiu, A.C., Gmal Osman, M., Strejoiu, C.V., and Lazaroiu, G., 2023. A comprehensive overview of photovoltaic technologies and their efficiency for climate neutrality. *Sustainability*, 15(23), p.16297.
- Lee, D., Hwang, J.G., Lim, D., Hara, T., and Lim, S., 2016. Incident angle-and polarization-insensitive metamaterial absorber using circular sectors. *Scientific Reports*, 6(1), p.27155.
- Liao, S.H., Wang, C.H., Ke, P.X., and Yang, C.F., 2024. Using planar metamaterials to design a bidirectional switching functionality absorber—an ultra-wideband optical absorber and multi-wavelength resonant absorber. *Photonics*, 11(3), p.199.
- Lin, Y., Cui, Y., Ding, F., Fung, K.H., Ji, T., Li, D., and Hao, Y., 2017. Tungsten based anisotropic metamaterial as an ultra-broadband absorber. *Optical Materials Express*, 7(2), pp.606-617.
- Liu, K., Hu, H., Song, H., Zeng, X., Ji, D., Jiang, S., and Gan, Q., 2013. Wideangle and polarization-insensitive perfect absorber for organic photovoltaic layers. *IEEE Photonics Technology Letters*, 25(13), pp.1266-1269.
- Liu, K., Zeng, B., Song, H., Gan, Q., Bartoli, F.J., and Kafafi, Z.H., 2014. Super absorption of ultra-thin organic photovoltaic films. *Optics Communications*, 314, pp.48-56.
- Liu, N., Mesch, M., Weiss, T., Hentschel, M., and Giessen, H., 2010. Infrared perfect absorber and its application as plasmonic sensor. *Nano Letters*, 10(7), pp.2342-2348.
- Liu, X., Xia, F., Wang, M., Liang, J., and Yun, M., 2023. Working mechanism and progress of electromagnetic metamaterial perfect absorber. *Photonics*, 10(2), p.205.
- Liu, Y., Chen, Y., Li, J., Hung, T.C., and Li, J., 2012a. Study of energy absorption on solar cell using metamaterials. *Solar Energy*, 86(5), pp.1586-1599.
- Liu, Y., Gu, S., Luo, C., and Zhao, X., 2012b. Ultra-thin broadband metamaterial absorber. *Applied Physics A*, 108, pp.19-24.
- Long, C., Yin, S., Wang, W., Li, W., Zhu, J., and Guan, J., 2016. Broadening the absorption bandwidth of metamaterial absorbers by transverse magnetic harmonics of 210 mode. *Scientific Reports*, 6(1), p.21431.
- Moniruzzaman, M., Islam, M.T., Muhammad, G., Singh, M.S.J., and Samsuzzaman, M., 2020. Quad band metamaterial absorber based on asymmetric circular split ring resonator for multiband microwave applications. *Results in Physics*, 19, p.103467.
- Musa, A., Alam, T., Islam, M.T., Hakim, M.L., Rmili, H., Alshammari, A.S., Islam, M.S., and Soliman, M.S., 2023. Broadband plasmonic metamaterial optical absorber for the visible to near-infrared region. *Nanomaterials (Basel)*, 13(4), p.626.
- Nguyen, T.Q.H., Nguyen, T.K.T., Cao, T.N., Nguyen, H., and Bach, L.G., 2020. Numerical study of a broadband metamaterial absorber using a single split circle ring and lumped resistors for X-band applications. *Aip Advances*,

- 10(3), p.035326.
- Padilla, W. J., and Fan, K., 2022. *Metamaterial Electromagnetic Wave Absorbers*. Springer Nature Switzerland AG, Switzerland.
- Prasada, N., Babua, T., Phanidharb, S., Singampallic, R., Naikd, B., Sarmaa, M., and Ramesha, S., 2021. Potential applications of metamaterials in antenna design, cloaking devices, sensors and solar cells: A comprehensive review. *Journal of Optoelectronic and Biomedical Materials*, 13(2), pp.23-31.
- Saadeldin, A.S., Sayed, A.M., Amr, A.M., Sayed, M.O., Hameed, M.F.O., and Obayya, S., 2023. Broadband polarization insensitive metamaterial absorber. *Optical and Quantum Electronics*, 55(7), p.652.
- Sayed, S.I., Mahmoud, K., and Mubarak, R.I., 2023. Design and optimization of broadband metamaterial absorber based on manganese for visible applications. *Scientific Reports*, 13(1), p.11937.
- Sayed, S.I., Mahmoud, K., and Mubarak, R.I., 2025. Circuit modeling and hybrid optimization of a lithography-free visible metamaterial absorber. *Discover Applied Sciences*, 7(8), p.790.
- Shen, G., Zhang, M., Ji, Y., Huang, W., Yu, H., and Shi, J., 2018. Broadband terahertz metamaterial absorber based on simple multi-ring structures. *Aip Advances*, 8(7), p.075206.
- Shen, Y., Pang, Y.Q., Wang, J.F., Ma, H., Pei, Z.B., and Qu, S.B., 2015. Ultrabroadband terahertz absorption by uniaxial anisotropic nanowire metamaterials. *IEEE Photonics Technology Letters*, 27(21), pp.2284-2287.
- Smith, D.R., Padilla, W.J., Vier, D., Nemat-Nasser, S.C., and Schultz, S., 2000. Composite medium with simultaneously negative permeability and permittivity. *Physical Review Letters*, 84(18), p.4184.
- Solak, E.K., and Irmak, E., 2023. Advances in organic photovoltaic cells: A comprehensive review of materials, technologies, and performance. *RSC Advances*, 13(18), pp.12244-12269.
- Tak, J., Jin, Y., and Choi, J., 2016. A dual-band metamaterial microwave absorber. *Microwave and Optical Technology Letters*, 58(9), pp.2052-2057.
- Takashima, Y., Furuta, S., Nagamatsu, K., Haraguchi, M., and Naoi, Y., 2024. Broadband Ag/SiO₂/Fe/TiO₂ ultrathin planar absorber with a wide acceptance angle from visible to near-infrared regions. *Optical Materials Express*, 14(3), pp.778-791.
- Tegegne, N.A., Nchinda, L.T., and Krüger, T.P., 2025. Progress toward stable organic solar cells. *Advanced Optical Materials*, 13(4), p.2402257.
- Tuong, P.V., Park, J.W., Lam, V.D., Jang, W.H., Nikitov, S.A., and Lee, Y.P., 2013. Dielectric and Ohmic losses in perfectly absorbingmetamaterials. *Optics Communications*, 295, pp.17-20.
- Verma, A., and Meena, O., 2023. A Review of Metamaterial Absorber and its Absorption Techniques. In: 2023 IEEE International Students' Conference on Electrical, Electronics and Computer Science (SCEECS). IEEE, Bhopal, India, pp.1-6.
- Veselago, V., 1967. The electrodynamics of substances with simultaneously negative values of ε and μ . *Uspekhi Fizicheskikh Nauk*, 92(3), pp.517-526.
- Wang, B.X., 2016. Quad-band terahertz metamaterial absorber based on the combining of the dipole and quadrupole resonances of two SRRs. *IEEE Journal of Selected Topics in Quantum Electronics*, 23(4), pp.1-7.
- Wang, B.X., Xu, C., Duan, G., Xu, W., and Pi, F., 2023a. Review of broadband metamaterial absorbers: From principles, design strategies, and tunable properties to functional applications. *Advanced Functional Materials*, 33(14), p.2213818.
- Wang, B.X., Zhai, X., Wang, G., Huang, W., and Wang, L., 2014. Design of a four-band and polarization-insensitive terahertz metamaterial absorber. *IEEE Photonics Journal*, 7(1), pp.1-8.
- Wang, C.Y., Liang, J.G., Cai, T., Li, H.P., Ji, W.Y., Zhang, Q., and Zhang, C.W., 2019. High-performance and ultra-broadband metamaterial absorber based on mixed absorption mechanisms. *IEEE Access*, 7, pp.57259-57266.

- Wang, G.Z., and Wang, B.X., 2015. Five-band terahertz metamaterial absorber based on a four-gap comb resonator. *Journal of Lightwave Technology*, 33(24), pp.5151-5156.
- Wang, J., Lang, T., Hong, Z., Xiao, M., and Yu, J., 2021. Design and fabrication of a triple-band terahertz metamaterial absorber. *Nanomaterials*, 11(5), p.1110.
- Wang, L., and Karaaslan, M., 2023. *Advanced Metamaterials for Engineers*. IOP Publishing, Bristol, UK, pp.358.
- Wang, P., Gao, Z., Xu, Z., and Zhao, T., 2023b. Perfect solar absorber based on four-step stacked metamaterial. *Photonics*, 10, p.1082.
- Wang, Q., Wang, Y., Tang, X.-Z., Huang, X., Xiong, Y., and Zhang, F., 2018. Analysis of triple-band binary metamaterial absorber based on low-permittivity all-dielectric resonance surface. *Journal of Advanced Dielectrics*, 8(3), p.1850021.
- Wen, D.E., Yang, H., Ye, Q., Li, M., Guo, L., and Zhang, J., 2013. Broadband metamaterial absorber based on a multi-layer structure. *Physica Scripta*, 88(1), p.015402.
- Wen, Q.Y., Zhang, H.W., Xie, Y.S., Yang, Q.H., and Liu, Y.L., 2009. Dual band terahertz metamaterial absorber: Design, fabrication, and characterization. *Applied Physics Letters*, 95(24), p.241111.
- Xie, J., 2023. Broadband Absorber Using Double-Layer Frequency Selective Surface Loaded with Resistors. New Materials, Machinery and Vehicle Engineering. IOS Press, Amsterdam, Netherlands, pp.180-186.
- Ye, Y.Q., Jin, Y., and He, S., 2010. Omnidirectional, polarization-insensitive and broadband thin absorber in the terahertz regime. *Journal of the Optical Society of America B*, 27(3), pp.498-504.
- Yu, P., Besteiro, L.V., Huang, Y., Wu, J., Fu, L., Tan, H.H., Jagadish, C., Wiederrecht, G.P., Govorov, A.O., and Wang, Z., 2019. Broadband metamaterial absorbers. *Advanced Optical Materials*, 7(3), p.1800995.
- Yue, S., Hou, M., Wang, R., Guo, H., Hou, Y., Li, M., Zhang, Z., Wang, Y., and Zhang, Z., 2020. Ultra-broadband metamaterial absorber from ultraviolet to long-wave infrared based on CMOS-compatible materials. *Optics Express*, 28(21), pp.31844-31861.
- Zhang, C., Zhou, W., Sun, S., Yi, N., Song, Q., and Xiao, S., 2015. Absorption enhancement in thin-film organic solar cells through electric and magnetic resonances in optical metamaterial. *Optical Materials Express*, 5(9), pp.1954-1961.
- Zhang, H., Yang, J., Zhang, H., and Liu, J., 2018. Design of an ultra-broadband absorber based on plasma metamaterial and lumped resistors. *Optical Materials Express*, 8(8), pp.2103-2113.
- Zhang, Y., Yang, W., Li, X., and Liu, G., 2023. Design and analysis of a broadband microwave metamaterial absorber. *IEEE Photonics Journal*, 15(3), pp.1-10.
- Zhao, C., Jia, M., Zhang, N., Meng, S., and Tian, Y., 2025. Ultra-wideband optically transparent flexible metamaterial absorber for satellite stealth. *Scientific Reports*, 15(1), p.29093.
- Zheng, H., Pham, T.S., Chen, L., and Lee, Y., 2023. Metamaterial perfect absorbers for controlling bandwidth: Single-peak/multiple-peaks/tailored-band/broadband. *Crystals*, 14(1), p.19.
- Zhou, Z., Zhou, X., Zhang, R., Ke, S., Zhu, W., Wu, S., Qin, L., and Li, X., 2023. Large-Area and Wide-Angle Perfect Absorbers based on Array of Nanospheres. In: *Nanophotonics, Micro/Nano Optics, and Plasmonics VIII*. SPIE, China, pp.191-201.
- Zhu, J., Ma, Z., Sun, W., Ding, F., He, Q., Zhou, L., and Ma, Y., 2014. Ultra-broadband terahertz metamaterial absorber. *Applied Physics Letters*, 105(2), p.021102.
- Zhu, W., 2018. Electromagnetic Metamaterial Absorbers: From Narrowband to Broadband. Intechopen, London, pp.133-151.
- Ziolkowski, R.W., 2006. Metamaterial-based source and scattering enhancements: From microwave to optical frequencies. *Opto-Electronics Review*, 14(3), pp.167-177.